Large Cation Engineering in Two-Dimensional Silver-Bismuth Bromide Double Perovskites

Large cation engineering in two-dimensional silver-bismuth bromide double perovskites

Fabian Schmitz,[1,2] Jonas Horn,[1,3] Nicola Dengo,[4] Alexander E. Sedykh,[1,5] Jonathan Becker,[1,5] Elena Maiworm,[2] Péter Bélteky,[6] Ákos Kukovecz,[6] Silvia Gross,[4,7] Francesco Lamberti,[4,7] Klaus Müller-Buschbaum,[1,5] Derck Schlettwein,[1,3] Daniele Meggiolaro,[8*] Marcello Righetto,[9*] Teresa Gatti[1,2*]

[1] Center for Materials Research, Justus Liebig University, Heinrich Buff Ring 16, 35392 Giessen, Germany

[2] Institute of Physical Chemistry, Justus Liebig University, Heinrich Buff Ring 17, 35392 Giessen, Germany

[3] Institute of Applied Physics, Justus Liebig University, Heinrich Buff Ring 16, 35392 Giessen, Germany

[4] Department of Chemical Sciences, University of Padova, via Marzolo 1, 35131Padova, Italy

[5] Institute of Inorganic and Analytical Chemistry, Justus Liebig University Heinrich-Buff-Ring 17, 35392 Giessen, Germany

[6] Interdisciplinary Excellence Centre, Department of Applied and Environmental Chemistry, University of Szeged, Rerrich Béla tér 1, H-6720 Szeged, Hungary

[7] Interdepartmental Centre Giorgio Levi Cases for Energy Economics and Technology, University of Padova, via Marzolo 9, 35131 Padova, Italy

[8] Computational Laboratory for Hybrid/Organic Photovoltaics (CLHYO), Istituto CNR di Scienze e Tecnologie Chimiche "Giulio Natta" (CNR-SCITEC), Via Elce di Sotto 8, 06123 Perugia, Italy

[9] Department of Physics and Astronomy, University College London, London WC1E 6BT, UK

Correspondence to: daniele.meggiolaro@cnr.it ; m.righetto@ucl.ac.uk ; teresa.gatti@phys.chemie.uni-giessen.de

Abstract

Double perovskites are promising candidates for less toxic and highly stable metal halide perovskites, but their optoelectronic performances still lag behind those of the lead halide counterpart, due to the indirect nature of the bandgap and the strong electron-phonon coupling. Reducing the dimensionality of $Cs_2AgBiBr_6$ down to a 2D layered form is strategic in order to tune the band gap from indirect to direct and provides new insights into the structure-property relationships of double perovskites. Herein, we report on a series of monolayer 2D hybrid double perovskites of formula $(RA)_4AgBiBr_8$, where RA represents different primary ammonium large cations with alkyl- and aryl-based functionalities. An in-depth experimental characterization of structure, film morphology and optical properties of these perovskites is carried out. Interestingly, the variation of the ammonium cation and the inter-planar distance between adjacent inorganic monolayers has peculiar effects on the film-forming ability and light emission properties of the perovskites. Experiments have been combined with DFT calculations in order to understand the possible origin of the different emissive features. Our study provides a toolbox for future rational developments of 2D double perovskites, with the aim of narrowing the gap with lead halide perovskite optoelectronic properties.

1. Introduction

Lead halide perovskites have revolutionized the semiconductor field due to their excellent optoelectronic properties, such as the direct band gap, the high absorption coefficient and the long lifetime of photo-generated charge carriers.[1–3] These properties have been mainly exploited in solar cell devices, where efficiencies beyond 25% have been reached in relatively few years.[4] Despite these outstanding efficiencies, toxicity issues related to the presence of lead[5] and the limited resistance against external agents, e.g. moisture,[6,7] have led to search alternative metals possibly replacing lead.

Within this context, 'elpasolites' or double halide perovskites (DHPs) hold great promise due to their excellent stability against environmental degradation.[8] In these materials, such as $Cs_2AgBiBr_6$, lead cations are replaced by iso-electronic metal cation pairs (i.e., mono- and tri-valent metal cations) arranged in alternating [$AgBr_6$] and [$BiBr_6$] octahedra. The valence band arises from Ag d^{10} and Bi s^2 orbitals, resulting in a relatively deep valence band, heavy hole masses and an indirect bandgap of ~ 2 eV.[9–11] Despite the excellent stability, the indirect nature of the band gap, as well as its relatively wide value, strongly limits their applications in outdoor photovoltaics. On the other hand, interesting and useful applications[12] have been identified for these species in other fields, such as photocatalysis,[13] transparent,[14] indoor[15] and, in general, building-integrated photovoltaics[16] and radiation detection.[17] The reduction towards two-dimensional (2D) monolayers, however, is an effective strategy to tune the band gap from indirect to direct,[18–20] thus opening new perspectives in the applications of DHPs in efficient optoelectronic devices.[21,22]

The synthesis of (001)-oriented 2D layered perovskites is achieved by introducing bulkier organic cations (e.g., featuring primary ammonium groups) and organic moieties, whose size cannot fit the octahedral cavities in the 'elpasolite' structure. The resulting structure is layered, and these large organic cations form bilayers that define the space between adjacent metal-halide octahedra-based inorganic planes.[23] In particular, DHPs (001) monolayers have formula $A'_4B^IB^{III}X_8$ and a handful of silver-bismuth versions have been recently reported, based on organic cations such as *n*-butyl[21] and *n*-propyl[24] ammonium or more complex ones such as phenylethylammonium[25,26] or dicationic 5,5′-diylbis(ammoniumethyl)-[2,2′-bithiophene], in line with the many structural variations carried out on the lead-based counterparts[27] and demonstrating the high versatility of the system.

The above-mentioned studies revealed that subtle structural details (e.g., distortion at the Ag site[28]) play a crucial role in determining the properties of the 2D DHPs. For instance, Connor et al.[21] reported significant changes in the electronic structure of distorted and non-distorted

$BA_4AgBiBr_8$. Although this could, in principle, provide control over the properties of these materials to a greater extent, much effort is needed in exploring the space of possible large cations and determining the resulting properties of the corresponding 2D DHPs.

In this study, we performed a systematic investigation of the effects of different aliphatic and aromatic ammonium cations on the structural and optoelectronic properties of the 2D $RA_4AgBiBr_8$ layered perovskites. The study has been focused on a selected list of RA organic cations that constitute the spacer between adjacent 2D inorganic layers, i.e. the aliphatic *n*-butylammonium (BA), isobutylammonium (iBA), hexylammomium (HA) bromides, featuring two different lengths for the linear alkyl chain and a branched one, and the aromatic phenylethylammonium (PEA) bromide. An in-depth characterization of the structure and morphology of perovskite polycrystalline films is carried out, revealing new insights into the solid-state organization of these hybrid compounds. Then, the impact of different cations on the optical properties of the perovskites has been investigated by optical spectroscopy and density functional theory (DFT) calculations. Interestingly, our analysis shows that change in the monolayer spacing induced by the different cations leads to different film morphologies that may tune selectively sub-bandgap PL emission associated with self-trapping of charge carriers in the 2D moiety.

2. Results and Discussion

2.1 Synthesis and structural properties

The four $A'_4AgBiBr_8$ compounds [henceforth referred to as $(RA)_4AgBiBr_8$] investigated in this work were produced employing the hydrothermal synthesis method reported in the Experimental Section. RA organic cations form *in-situ* during the synthetic process from the corresponding amines and hydrobromic acid. The structure of the final compounds is sketched for two layers of alternating [$AgBr_6$] and [$BiBr_6$] octahedra in Figure 1a. We obtained four different compounds for the different larger cations as four crystalline powders of yellow color, mainly comprising platelet-like crystals of lateral sizes up to 100 µm (see Figure S1 in the Supporting Information – S.I. - for an example), that we directly used for powder x-ray diffraction (P-XRD). In Figure 1b, we show the diffractograms for the synthesized samples. A marked difference between the parent 3D structure of $Cs_2AgBiBr_6$ (green diffractogram), and the layered $(RA)_4AgBiBr_8$ compounds can be observed from the presence of intense (001) reflections at 2θ values below 10°. We ascribe these reflections to the periodic spacing between adjacent 2D inorganic sheets created by the large organic cation bilayers. From the position of

these reflections, the (001) lattice distance (d_{001}) can be calculated by applying Bragg´s law (Table 1).

Table 1. 2θ values of the first (001) reflections in P-XRD of Figure 1b and calculated (001) lattice constants.

Compound	2θ (°)	d_{001} (Å)
$(BA)_4AgBiBr_8$	6.7	13.2
$(iBA)_4AgBiBr_8$	6.7	13.2
$(PEA)_4AgBiBr_8$	5.5	16.2
$(HA)_4AgBiBr_8$	5.1	17.4

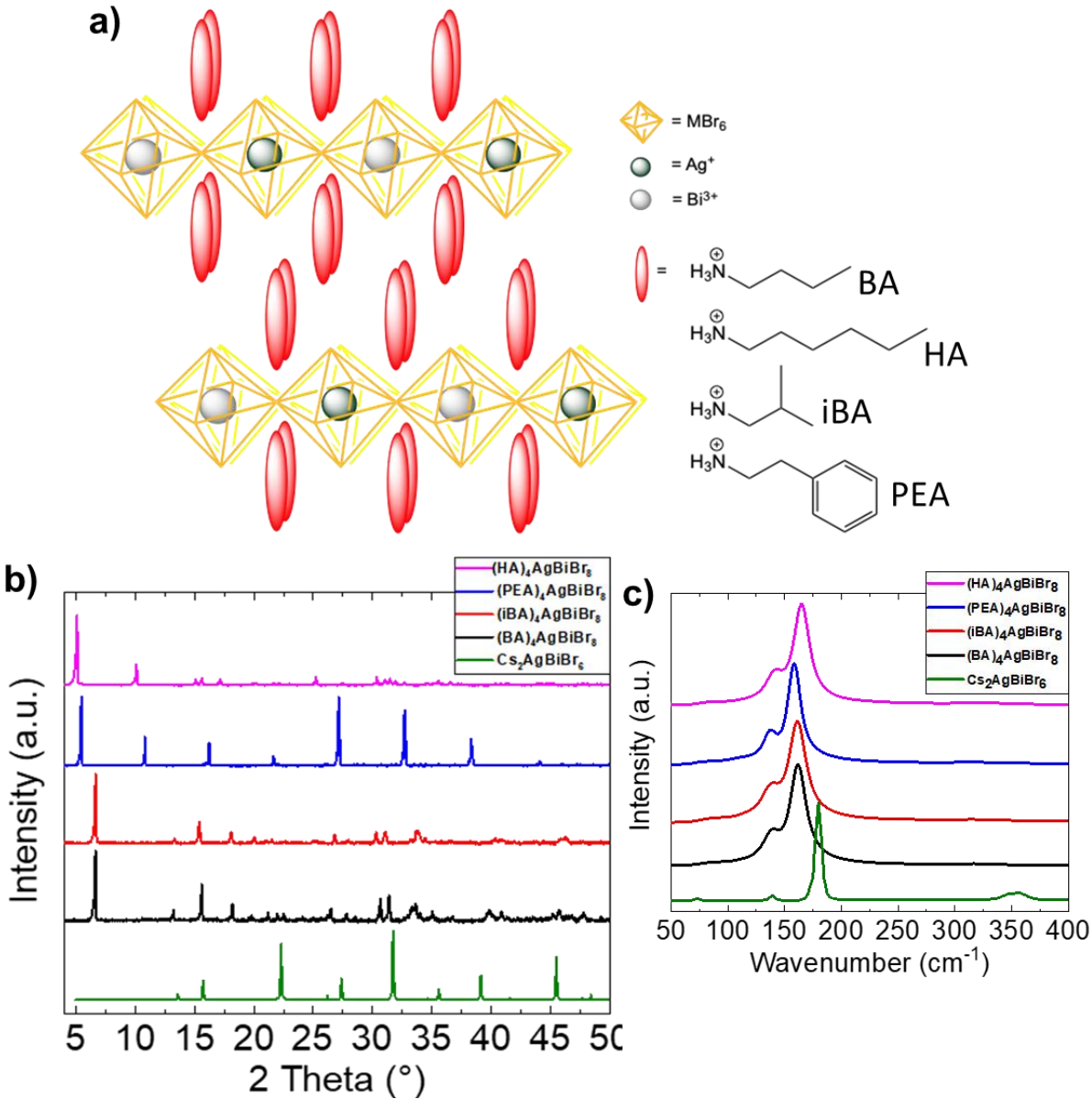

Figure 1. a) Sketch of the structure of 2D hybrid silver-bismuth double perovskites of general formula $(RA)_4AgBiBr_8$. b) P-XRD patterns of the four hydrothermally synthesized $(RA)_4AgBiBr_8$ crystalline compounds and of the reference 3D double perovskite $Cs_2AgBiBr_6$. c) Low wavenumber region of the Raman spectra of the four $(RA)_4AgBiBr_8$ compounds and the reference 3D double perovskite $Cs_2AgBiBr_6$.

P-XRD data reveal how large cations affect the geometry of the resulting structure in the first instance. The large cation structure allows the fine-tuning of the spacing distance between the adjacent inorganic sheets. While moving from a linear to a branched alkyl moiety (BA to iBA) does not significantly affect such spacing, longer alkyl chains (HA) and bulkier groups (PEA) effectively increase the spacing. In comparison with others, the $(PEA)_4AgBiBr_8$ sample shows an anomalous P-XRD pattern dominated by the regular reflections belonging to the <00l> family up to (008). This could be related to a very regular 2D stacking order in the structure (i.e. large numbers of PEA double layers are stacked in an ordered way in the crystals), as was observed previously for a lead-based 2D perovskite.[29]

The dimensional reduction in the four hybrid double perovskites further emerges when tracking the behavior of the most intense phonon mode in the Raman spectra of these compounds in comparison to that of the 3D reference $Cs_2AgBiBr_6$. Figure 1c shows the low wavenumber region of these spectra, dominated by the longitudinal optical A_{1g} mode (symmetric in-phase stretching of the Bi–Br and Ag–Br bonds in the $Ag/BiBr_6$ layers).[30] This phonon mode is located at 177 cm^{-1} for the 3D double perovskite (green line), while shifts to lower wavenumbers in all the three 2D hybrid compounds (at 161, 161, 158 and 165 cm^{-1} for, respectively, RA = BA, iBA, PEA, HA), still maintaining the highest intensity among all other features within the spectrum (see Figure S2 in the S.I. for the high wavenumber region, featuring the organic cations vibrational modes). Therefore, the loss of the third dimension in the overall metal-halide octahedra connectivity, which is determined by the generation of the layered species, diminishes the phonon mode energy. Due to the nature of the A_{1g} mode, the phonon softening phenomena observed might be related to weaker Bi-Br and Ag-Br bonds, as a consequence of the loss of the octahedra connectivity in the third dimension for the layered structures (see further discussion in Figure S3 of the S.I.). Interestingly, the shift appears to be not strictly correlated to the interplanar distance measured via P-XRD, therefore it cannot be attributed to the mere variation of spacing between layers. There is also no strict correlation to the dipole moment of the organic cations (Table 2, *vide infra*), which could have an influence

on the electronic distribution in the Br^- ions close to the polar head of the organic cations. Recently, Li et al. have demonstrated how distortions of the inorganic framework inducted by organic A-cation soften the lattice of layered lead halide perovskite and result in lower phonon energies.[31] Therefore, we can only speculate that this shift is influenced by the intermolecular packing of organic tail groups and, hence, mechanical flexibility of the different organic interlayers. Nevertheless, we believe that further studies are needed to fully understand the role of organic large cations of the vibrational properties of the inorganic lattice in layered perovskites.

Attempts to grow single crystals suitable for X-ray diffraction (SC-XRD) of the iBA, PEA and HA 2D monolayer double perovskite derivatives (for the BA derivative, single-crystal details can be found in ref.[21]) were successful in only one case, i.e. $(PEA)_4AgBiBr_8$. We attribute the unsuccessful obtainment of SC structures for iBA and HA-based 2d DHPs to the extreme disorder present in these structures. Reasonable diffraction intensities could not be obtained with sufficient resolution for structure solution or refinement, which is most likely because the organic cations exhibit consistent disorder (we were successful in crystallizing a structure with BA, but this structure was already reported[21]). The experimental details used for inducing such a crystallization process are reported in the Experimental Section. A crystal structure for the $(PEA)_4AgBiBr_8$ compound was already deposited in the Cambridge database, but with a different level of refinement and only to predict the P-XRD patter for the identification of side phases formed in parallel to a bilayer analogous:[32] on the contrary here we present a detailed description of the structure, which will be helpful for gaining further insights into structure-property relationships existing both in this compound and similar ones (a new structure has been deposited in the database, see details in the Experimental Section). SC-XRD analysis of the structure of $(PEA)_4AgBiBr_8$ reveals a typical monolayer DHP structure with a regular alternation of Ag^+ and Bi^{3+} sites within the inorganic sheets, which are separated by a distance of 16.15 Å (Figure 2a), thus strongly supporting the information obtained from P-XRD. The space group is $P\bar{1}$ (see table S1 in the S.I. for the summary of crystallographic data and structure refinement) and the unit cell is defined by four in-plane corner-sharing metal bromide octahedra (two Bi-based and two Ag-based) and eight PEA cations (Figure 2a and S3 in S.I.). The latter was found to be disordered over three positions. Such structural variability also exists for the position of the equatorial bromide atoms (with a conformation that occurs prevalently -91.3%- and a less common one -8.7%-).

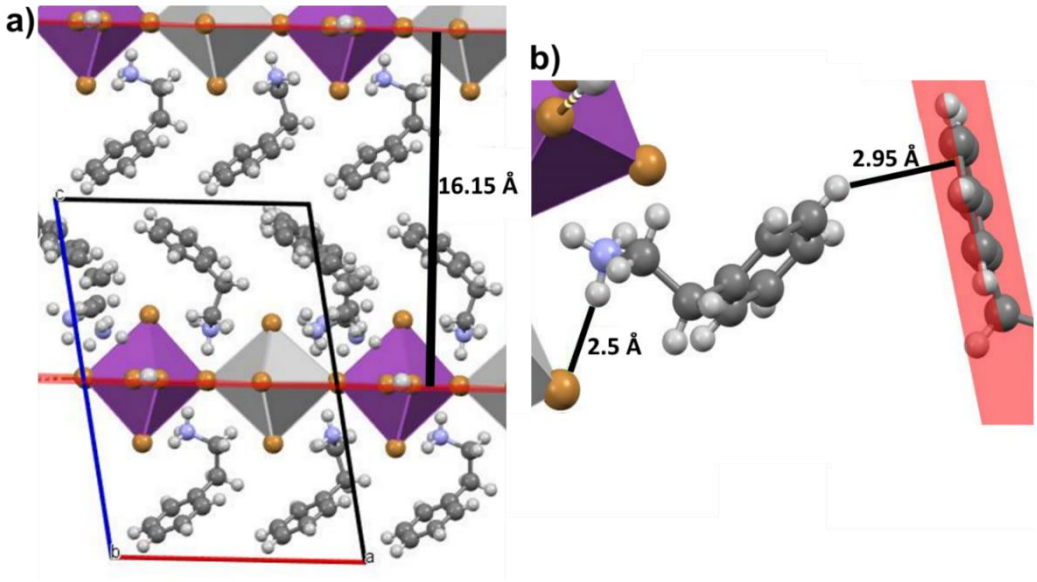

Figure 2. Details of the single-crystal structure of $(PEA)_4AgBiBr_8$. a) View along the b-axis with indicated the interplanar distance between two adjacent inorganic monolayers of metal-bromide octahedra (taken between the planes containing the equatorial bromides). b) View of the herringbone motif established within the phenylethylammonium-based organic bilayer that highlights the stabilizing CH-π interactions (in red the plane that contains the benzene ring). The hydrogen bond between an ammonium group and a bromide ion is also evidenced (shortest contact of three possible ones).

In Figure S4 of S.I. the heavily distorted geometry of the inorganic monolayers can be clearly observed, with angles between the bismuth- and silver-based octahedra in a square unit of 68° and 112°. Interestingly, the tetragonal distortion at the $[AgBr_6]$ sites observed by Connor et al.[21] in that of $(BA)_4AgBiBr_8$ is not clearly observed in our data on $(PEA)_4AgBiBr_8$. However, the uncertainty associated with the silver-bromide distance could contribute to detecting similar equatorial and axial metal-bromide distances (Figure S5). We further examined the SC-XRD data in the search for stabilizing interactions existing at the level of the organic bilayer. Here, the periodic arrangement of the phenyl rings is reminiscent of the classic herringbone motif present, for example, in crystals of the acenes series.[33,34] Within this arrangement, CH-π interactions between edge-to-face arranged aromatic rings play a significant role in driving the formation of such an overall disposition of molecules within the crystal. Figure 2b illustrates a detail of this structural feature, with an estimated CH-π distance of 2.95Å, therefore in the order of distances typical for this type of van der Waals intermolecular interactions.[35] This stabilizing effect of the π electron density and its interactions, not present in the other compounds

investigated in this work, might at least partially explain the slightly higher thermal stability of $(PEA)_4AgBiBr_8$ compared to $(BA)_4AgBiBr_8$, $(iBA)_4AgBiBr_8$ and $(HA)_4AgBiBr_8$ that is seen in the thermograms reported in Figure S6 of the S.I.

The structural properties of the four hydrothermally synthesized 2D DHP crystalline compounds were further examined through high-resolution transmission electron microscopy (HR-TEM). All samples presented two different types of populations: one characterized by relatively thin crystalline flakes and one constituted of darker (and thus thicker) regions (see Figures S7-S10 in the S.I.). Selective area diffraction (SAED) carried out on both the flake-like and darker regions show analogous patterns within each different sample and allows extracting the average in-plane lattice constant for all the four 2D DHPs examined (see Figure S11 in the S.I.).[36] We extracted nearly identical values around 8 Å for all the four species (see information on rings 1 inserted as tables in Figure S11 for each SAED pattern). Considering that these are not images taken in cross-section on the crystalline species and thus do not highlight the layered structure, we can safely assign this to repetitive features within the planes of the 2D inorganic sheets, such as the diagonal distance between identical metal centers. This can be verified further for the $(BA)_4AgBiBr_8$ and $(PEA)_4AgBiBr_8$ compounds for which single-crystal structural data are available. From micrographs taken at higher magnifications, we can also distinguish periodic motifs (also shown in Figures S7-S10), characterized by distances that vary from 2.7 to 3.8 Å. We assign these features to in-plane metal-halide distances within the inorganic sheets. To further investigate the structure of these powders, we carried out energy dispersive x-ray analysis (EDX) characterization on a selected sample, i.e. $(BA)_4AgBiBr_8$. Notably, measurement for the two types of populations described above (Figure S12) qualitatively indicate that depletion of silver cations characterizes the first population (orange frame). In contrast, the second (red frame) contains both bismuth and silver. These observations indicate that our powder samples have some degree of heterogeneity and a more complex identity than what could be inferred by merely focusing on P-XRD patterns. For instance, the presence of a Bi- only side phase cannot be inferred from that analysis (we exclude the presence of residual un-reacted $BiBr_3$, as there is no trace of its reflexes in the P-XRD). On the other hand, it is known for the case of the 3D double perovskite $Cs_2AgBiBr_6$ that often a bismuth-rich impurity can form either during hydrothermal synthesis or during thin film deposition (the species with formula $Cs_3Bi_2Br_9$, which cannot be present here as no Caesium ions were introduced during the hydrothermal synthesis of the 2D monolayer DHPs),[9] therefore it seems reasonable to guess that the here identified sample regions lacking silver could be a 2D-version

of this bismuth-based compound or some analogous ones that are up to now unreported in literature, to the best of our knowledge.

2.2 Thin-films morphology

The four hydrothermally synthesized 2D DHP derivatives were cast into thin-films onto glass substrates. The detailed procedure of the process is provided in the Experimental Section. Briefly, $(RA)_4AgBiBr_8$ crystalline powders were dissolved in DMF and subsequently spun on a glass/FTO substrate and annealed. Thin-film XRD (Figure S13 in the S.I.) reveals the formation of highly preferentially oriented crystalline phases.[37] Differently from the P-XRD spectra, the intensity of the first reflection at low 2θ values, in all cases significantly more intense than all other reflections, suggests that the crystalline phases are growing parallel to the substrate. Similar behavior has already been reported for 2D lead halide perovskites.[38] On the other hand, the position of this reflection is unvaried with respect to the one in P-XRD (Figure 1b). Therefore, thin-film XRD confirms that the interplanar distance among 2D inorganic sheets is maintained and governed by the length and stereochemistry of different organic cations. The four resulting yellow thin films appeared to have different textures already at the naked eye (photos are visible in Figure S14): BA and PEA-based films are smooth and homogeneous, the iBA-based film is translucent, and the HA-based has a wax-like character with a non-homogeneous distribution on the substrate. Scanning electron microscope (SEM) analysis of thin films prepared on FTO in top-view imaging mode (Figure 3) reveals the microstructure of the four different films.

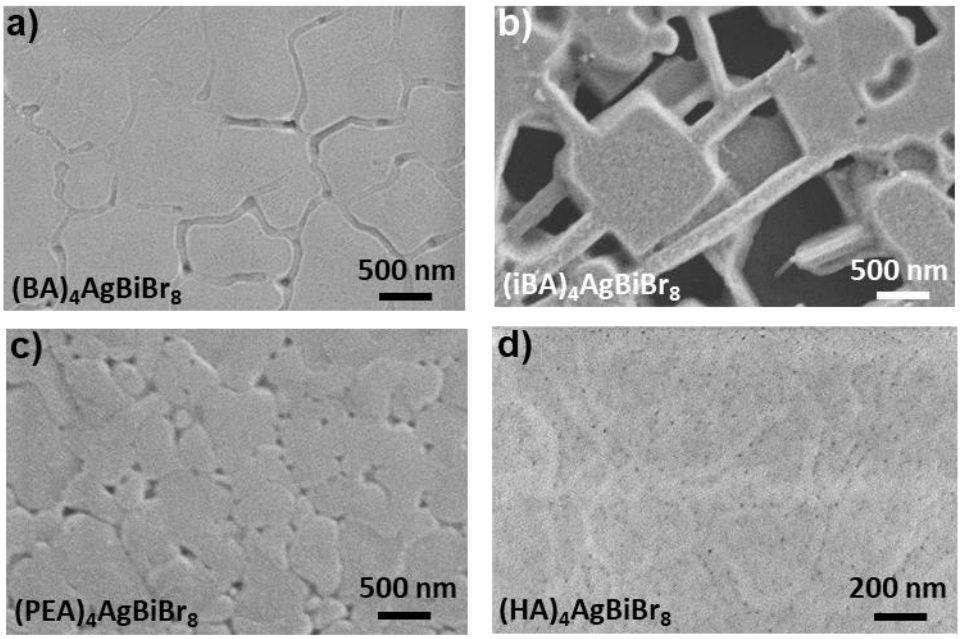

Figure 3. Top-view SEM images of spin-coated thin films of a) $(BA)_4AgBiBr_8$, b) $(iBA)_4AgBiBr_8$, c) $(PEA)_4AgBiBr_8$ and d) $(HA)_4AgBiBr_8$ on top of FTO substrates.

Here, the film obtained from $(BA)_4AgBiBr_8$ shows a relatively flat surface, where some valleys emerge most likely as an effect of the evaporating solvent. $(PEA)_4AgBiBr_8$ thin films show a similar, yet more grain-like morphology, with some pinholes.[39] The $(HA)_4AgBiBr_8$ films appear uniform, with many small pinholes. It is worth noting that this is also the thinnest among all the four films examined (see Figure S15 for cross-section SEM images). The appearance of the $(iBA)_4AgBiBr_8$ film is undoubtedly the most peculiar one: micron-sized square-like features have grown during film casting, which are connected one to the other by thinner and longer filaments while leaving around consistent amounts of empty space. This highly micro-structured morphology, most likely characterized by a relatively high surface area, could be the reason for the opaque visual appearance of the thin film (Figure S14) as a result of light scattering.

Surface morphologies of the thin films were analyzed in details through atomic force microscopy (AFM) in tapping mode, with peculiar images obtained for the $(BA)_4AgBiBr_8$ and $(PEA)_4AgBiBr_8$ based samples. The topography scans on the two thin films are reported in Figure S16, accompanied by line-profiles taken in the area of the surface indicated by black lines and numbers. From the $(BA)_4AgBiBr_8$ topography scan, we recognize the presence of many nanometric areas within the main grains, located at a lower height compared to the top smooth surface. When measuring the depth of these areas through depth profiling (right-hand side graphs), we observe that the step corresponds with a good approximation to a single interplanar distance among the 2D inorganic sheets in the layered perovskite (see Table 1). The same can also be inferred for the $(PEA)_4AgBiBr_8$ film (where not only monolayer steps are present but also bilayer ones, as can be seen in relative profile n. 1), even if for this species the surface topography is not flat but rather discontinuous, likely as a result of the more random orientation of the (001) crystallites in the film[40] (which still on average displace mainly parallel to the substrate, as suggested by thin-film XRD). The high tendency to form the inorganic sheets separated by the organic cations is shown by the formation of the terraces in all cases. Dynamic light scattering (DLS) analysis of the solutions used to produce the films (Figure S17) show the presence of scattering particles with diameters of several hundred nm (in most cases, only one distribution of diameters is found, whereas in the case of $(BA)_4AgBiBr_8$ two distributions result). Hence, we hypothesize that when these crystals are dispersed in a highly coordinating solvent, they disassemble into single or few-layers inorganic sheets. Once cast

into thin films, these solutions produce a more ordered stacking, which is reminiscent of a layer-by-layer assembly driven by the evaporation of the solvent.[38] Notably, the growth of thin films can therefore be described as a self-assembly process of pre-existing colloidal species[41] rather than a complete dissolution and re-growth process. This interpretation is confirmed by the fact that similar films could not be prepared from mixed solutions of metal- and ammonium bromides. Figure S18 reports the AFM studies carried out on the iBA and HA-based DHP films. Here, we observe an analogous step-like topography, albeit with much higher steps (around 10 nm) for iBA. These steps correspond to multilayer structures protruding from the surface. In addition, the influence of the cation on the thin film morphology is further confirmed by comparing the surface roughness obtained from AFM measurements (Figure S16 and S18). While the $(HA)_4AgBiBr_8$ film is very flat (RMS 2.1 nm), thin films of $(PEA)_4AgBiBr_8$ and $(BA)_4AgBiBr_8$ are slightly rougher (RMS 4.2 nm) and the $(iBA)_4AgBiBr_8$ film shows a considerably increased surface roughness (RMS 34.1 nm).

Similar to the structural diversity found in the thin film morphology of the four compounds we observed a variability of their work function (WF), as measured by Kelvin probe force microscopy (KPFM), shown in Figure 4 and Table 2. The different WF can be directly correlated to the dipole moment calculated for the organic cations RA^+ (Figure S19). The observed work function decreases with the calculated dipole moment of RA^+, well compatible with an orientation of the positive end of the dipole (NH_3^+-group) towards the inorganic sheet and the negative (organic) end towards vacuum, leading to the observed lowered WF. Such direct correlation of the observed WF with μ of the RA^+ reveals an organic termination of the surface. This is also indicated by very similar[42] band structures calculated for $(PEA)_4AgBiBr_8$ and $(BA)_4AgBiBr_8$ despite significant differences in the surface WF of these materials (Table 2). Interestingly, for the layered lead-based perovskite $(PEA)_2PbI_4$ an almost identical WF of 4.87 eV was reported[42] as we find for $(PEA)_4AgBiBr_8$, confirming that the organic moiety dominates the work function of the surface rather than the underlying inorganic sheets.[43] By looking at the FWHM of the WF signals, we find a considerably broader distribution for $(BA)_4AgBiBr_8$ which hints at a lower degree of order of the organic layer when compared to the three other organics, where a stronger inter-molecular interaction can be expected that would lead to a higher degree of order and, hence, smaller FWHM of the WF.

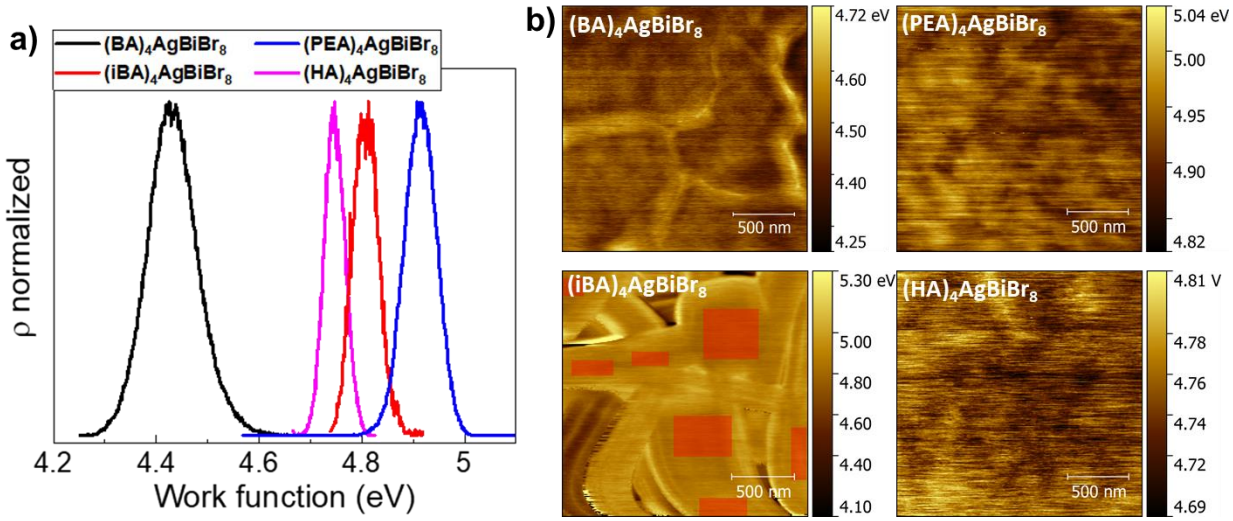

Figure 4. a) Distribution of work function of the investigated $(RA)_4AgBiBr_8$ thin films. Every histogram contains at least two KPFM measurements, one of which is shown in b) for each compound. For $(iBA)_4AgBiBr_8$, only the marked regions were evaluated to avoid an influence of the strongly stepped morphology, whereas the whole area was evaluated for the other three compounds.

Table 2. Work function (WF) and FWHM obtained by Gauss fits of the distribution (Figure 4a) for the four $(RA)_4AgBiBr_8$ and calculated dipole moments μ of the organic cations RA^+

Compound	WF (eV)	FWHM (eV)	μ (D)
$(BA)_4AgBiBr_8$	4.43	0.11	1.583
$(HA)_4AgBiBr_8$	4.75	0.05	1.330
$(iBA)_4AgBiBr_8$	4.81	0.06	1.173
$(PEA)_4AgBiBr_8$	4.91	0.07	0.947

2.3 Optical properties and computational modelling

The optical properties of thin films have been investigated by absorption and PL spectroscopy (see results in Figure 5a). The UV-Visible absorption spectra of the thin film series show well-defined transitions at around 3 eV. Gaussian fitting analysis (Figure 5a, Table 3) reveals that the observed absorption bandwidths have an FWHM larger (up to 380 meV) than for $Cs_2AgBiBr_6$ (about 200 meV, as taken from previous work of some of us[10]). Furthermore, $(iBA)_4AgBiBr_8$ thin films present an additional peak at 2.83 eV.[44,45] These observations suggest the presence of multiple transitions, whose energy is finely controlled by the rotation of the octahedra and the length of the organic spacers.

The assignment of the parent 3D $Cs_2AgBiBr_6$ transition is crucial to understand and interpret the optical response of the 2D $(RA)_4AgBiBr_8$ series. It is well established that bulk $Cs_2AgBiBr_6$ has an indirect bandgap of 1.8-2.2 eV. As discussed by Palummo et al. by computational excited-state methods, the first absorption peak in bulk $Cs_2AgBiBr_6$ is the result of a bound exciton, while the PL spectrum derives from a phonon-assisted radiative recombination process of indirect bound excitons.[46] On the other hand, no consensus has been reached on the nature of the prominent resonant optical feature generally observed at around 2.8 eV.[10,30,47,48] Clarifying its assignment is even more critical for lower dimensional structures, where the 1D/2D confinement of $Cs_2AgBiBr_6$ converts the bandgap from indirect to direct character. Alivisatos et al. postulated a role played by bismuth ion intra-atomic $s \rightarrow p$ orbital transitions, whose spin-forbidden character is at least partially allowed by the strong spin-orbit coupling of bismuth.[44] On the other hand, Karunadasa et al., based on DFT calculations, suggested additional charge-transfer contributions from Ag-d to Bi-s/Bi-p orbitals.[21] In this context, the comparison between large cations in the $(RA)_4AgBiBr_8$ series provides further insight into the nature of this transition.

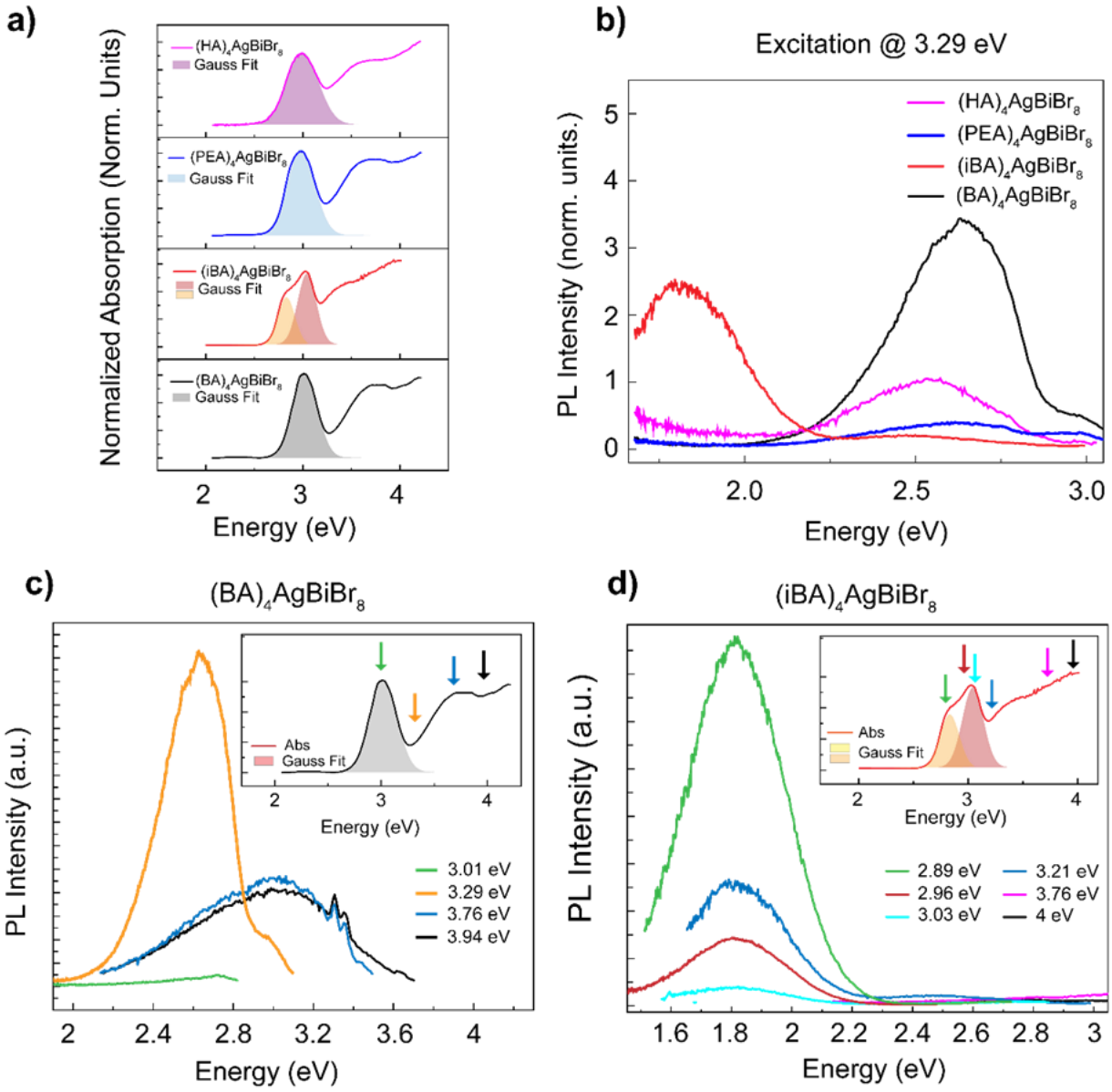

Figure 5. a) UV-Visible absorption spectra of $(RA)_4AgBiBr_8$ thin films (solid lines) and deconvoluted peaks (shaded areas) by gaussian fitting of the band-edge transitions. b) Normalized steady-state photoluminescence spectra of $(RA)_4AgBiBr_8$ thin films under 3.29 eV excitation measured at 77 K. Excitation energy-dependent PL spectra for c**)** $(iBA)_4AgBiBr_8$ and d) $(BA)_4AgBiBr_8$ thin films at 77 K. In the insets, the excitation wavelengths are indicated above the absorption profiles by colored arrows.

Table 3. Gaussian fitting results for main absorption and photoluminescence (under 3.29 eV excitation) of the $(RA)_4AgBiBr_8$ thin film series.

Thin-film	Absorption		Photoluminescence	
	Position (eV)	**FWHM (eV)**	**Position (eV)**	**FWHM (eV)**
$(BA)_4AgBiBr_8$	3.019±0.001	0.30	2.620 ± 0.002	0.37
$(iBA)_4AgBiBr_8$	2.827±0.002	0.21	1,820 ± 0.001	0.38
	3.041±0.001	0.22	2.470 ± 0.002	0.5
$(PEA)_4AgBiBr_8$	2.981±0.001	0.34	2.604 ± 0.002	0.53
$(HA)_4AgBiBr_8$	2.996±0.001	0.39	2.520 ± 0.002	0.44

To characterize optical fingerprints of the perovskite series more in detail, the diffuse reflectance has been measured and analyzed by Kubelka-Munk theory. The resulting Kubelka-Munk function F(R) spectra, equivalent to absorption spectra, are shown in Figure S20. Notably, the prominent absorption peak lies at ~ 3 eV and presents a similar shifting trend with different cations (see Table 3). However, the absorption edge is largely split with an additional peak at ~ 2.6 eV, with only minor differences among the cations. Karunadasa et al. observed a similar effect for $(BA)_4AgBiBr_8$ powders, but the authors reported only the band-edge.[21]

As shown in Figure 5b, the $(RA)_4AgBiBr_8$ thin films show significant emission peaks under 3.29 eV excitation. Specifically, the comparison (where PL data are normalized for the absorption at 3.29 eV) reveals how $(BA)_4AgBiBr_8$ and $(iBA)_4AgBiBr_8$ show the most intense emission. By comparing the integrated area (see Table S1), the intensity of $(PEA)_4AgBiBr_8$ and $(HA)_4AgBiBr_8$ is reduced with respect to BA-based perovskite by a factor of ~7 and ~3, respectively. All the samples share a broad emission peak at around 2.6 eV with FWHM ranging from 300 to 600 meV (see the normalized comparison in Figure S21). As reported in Table 3, the position of these peaks shifts with different cations from 2.62 eV for $(BA)_4AgBiBr_8$ to 2.47 eV for $(iBA)_4AgBiBr_8$. These results are in excellent agreement with the report by Karunadasa et al., where the emission was assigned to trap-mediated recombination.[21] Differently from other samples, $(iBA)_4AgBiBr_8$ also exhibits a broad (~ 400 meV) and highly intense emission band at 1.8 eV. The ratio between this emission and emission under 2.89 eV excitation is about 10, thereby indicating this as an efficient emission channel.

To further explore the excited states of these samples, we measured excitation energy-dependent PL spectra for $(BA)_4AgBiBr_8$ and $(iBA)_4AgBiBr_8$ (Figure 5c and 5d, respectively). The excitation energy dependence of the PL has already been used to reveal the underlying complex excited-state dynamics of several perovskite and emerging semiconductor systems,[49–51] yet there are no previous reports for 2D Ag-Bi DHPs. For $(iBA)_4AgBiBr_8$ thin films,

although the emission at 2.6 eV is clearly observed for above band-gap excitations (3.29 eV), resonance excitations (3.01 eV) result in a significantly quenched emission. Such behavior indicates the presence of an additional non-radiative recombination mechanism (e.g., trap mediated non-radiative recombination) strongly coupled with the central transition. Furthermore, the use of higher excitation energies produces a broad emission peaked at 3.1 eV. This emission violates the Kasha rule (i.e., the emission takes place from the lowest excited state) and can therefore be tentatively ascribed to the presence of high-lying states which are electronically decoupled from the lower-lying ones, e.g., high-lying trap states or self-trapped exciton (STE) states.[52,53] On the contrary, the emission of $(iBA)_4AgBiBr_8$ thin films under different excitation energies is always dominated by the emission at 1.8 eV. Notably, the intensity of the emission is strongly dependent on the excitation wavelength. Specifically, the emission quenching is observed in correspondence with the main absorption transition (3.01 eV), analogously to what observed for $(BA)_4AgBiBr_8$. Furthermore, the STE emission is fully quenched when excitation energies above 3.7eV are used. Powder emission PL spectra (Figure S21) confirm the presence of a higher energy emission peak for $(iBA)_4AgBiBr_8$, analogously to what was observed for $(BA)_4AgBiBr_8$.

To delve deeper into the origin of optical excitations in the perovskite series and confirm our assignments, we have selected the two isomeric layered perovskites, $(BA)_4AgBiBr_8$ and $(iBA)_4AgBiBr_8$ as model systems. Therefore, we have investigated their electronic and optical properties by ab-initio density functional theory (DFT) and many-body perturbation theory (MBPT). The electronic band structures and projected density of states of the (BA, $iBA)_4AgBiBr_8$ perovskites have been calculated at the DFT level by using the Perdew-Burke-Ernzherof (PBE) functional[54] and by including spin-orbit coupling (SOC, see Figure 6a-d).

In both cases cell and ion positions have been relaxed at the PBE level by including DFTD3 dispersions (see Computational details).[55] Upon structural optimization, a slight contraction of the $(iBA)_4AgBiBr_8$ cell along the z-axis is reported with respect to the parent $(BA)_4AgBiBr_8$ perovskite, due to the branched geometry of the iBA cation. The two systems show a similar electronic structure with direct band gaps at the Γ point of 1.59, and 1.66 eV for BA and iBA, respectively. A nearly two-fold degeneracy of electronic bands at the VBM and CBM is reported. The analysis of PDOS highlights that the VB is mainly composed by Br-p and Ag-d orbitals, while the CB mainly derives from Bi-p and Br-p hybridized orbitals with small components of Ag-s orbitals, in agreement with previous studies.[21] In both cases, organic cations do not contribute to the electronic states in the proximity of the band edges.

As expected, the calculated band gaps at the PBE-SOC levels strongly underestimate the absorption edges observed in optical experiments. To provide a more accurate estimate of the electronic band gap of these systems, G_0W_0 calculations[56] have been performed on the $BA_4AgBiBr_8$ perovskite by including SOC (see Computational details in the Experimental Section).

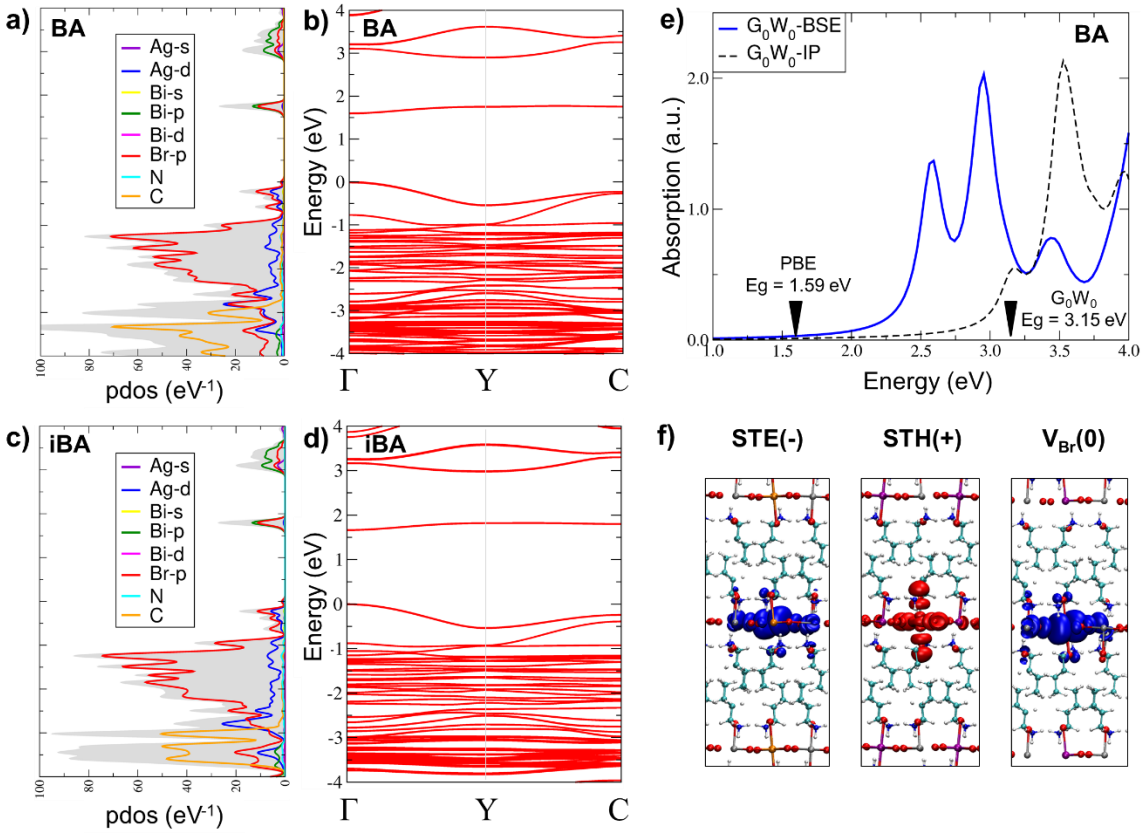

Figure 6. a) Electronic band structure and PDOS of a-b) $(BA)_4AgBiBr_8$ and c-d) $(iBA)_4AgBiBr_8$ layered perovskites, calculated at the PBE-SOC level of theory; e) optical absorption spectrum of $(BA)_4AgBiBr_8$ calculated at the G_0W_0-independent particle level (G0W0-IP) and by including exciton effects through the solution of the BS equation (G_0W_0-BSE); f) orbital plots of trapped charge carriers in $(BA)_2AgBiBr_8$: self-trapped electron (STE); self-trapped hole (STH); trapped-electron at the V_{Br} site.

Within the G_0W_0 approximation, a significant renormalization of the electronic band gap to 3.15 eV is obtained for $BA_4AgBiBr_8$. The optical absorption spectrum of the perovskite has been simulated at the G_0W_0-independent particle level (G_0W_0-IP) and by including exciton effects by solving the Bethe-Salpeter (BS) equation (G_0W_0-BSE)[57] on top of G_0W_0 corrected eigenvalues (Figure 6e). The solution of the BS equation leads to two main optical absorptions

peaks in the low energy range of the spectrum, centered at 2.58 eV and 2.96 eV. These excitations are mainly associated with transitions between the nearly degenerate levels of the VBM and the CBM, in the proximity of the Γ (0, 0, 0) and C (0.5, 0.5, 0.5) k-points in the Brillouin zone (BZ), respectively. The calculated absorption spectrum is in good agreement with the absorption profile extracted by the Kubelka – Munk analysis (see Figure S20). By considering the energy red-shift of the first exciton peak with respect to the calculated electronic gap, an exciton binding energy of 0.57 eV is estimated. Such value is naturally higher than in the $Cs_2AgBiBr_6$ bulk perovskite, where an exciton binding energy of 0.34 eV has been reported.[46] The presently observed increase in exciton binding energy and blue-shift by 200 meV in the absorption spectrum with respect to the bulk $Cs_2AgBiBr_6$ are due to a combined effect of dielectric confinement and octahedral distortion.[45] As widely reported for layered lead halide perovskites,[58] the confinement of the carriers arises not only from the restricted motion in a 2D plane (i.e., quantum confinement) but also from the reduced dielectric screening caused by the presence of organic cation layers with lower permittivity compared to 3D bulk (i.e., dielectric confinement).[19,20] Furthermore, as demonstrated by Radaelli et al. for $Cs_2AgBiBr_6$, the distortion in Br-Ag-Br angles strongly determines the energy of the direct gap transition.[48] Within this framework, the slight peak shift observed within the 2D perovskite series (i.e. from 2.98 up to 3.04 eV, see Figure 5a and Table 3) can be ascribed to distortions caused by the different steric hindrance of the large cations. These results, in combination with the very similar electronic structure found at the DFT level among the two perovskites, suggest that optical absorption peaks observed at ~2.7 and ~3.0 eV may be associated to exciton transitions, and a defect-related origin is likely to be excluded.

PL emissions in the low energy range, i.e. below the first estimated exciton peaks, such as emission at ~1.8 eV in iBA, are in principle related to emission from defects or self-trapped charge carriers. To investigate this possibility, charge carrier trapping in the perfect lattice and at bromide vacancies defect sites have been studied by performing DFT calculations in 2x2x1 supercells of BA and iBA systems. PL sub-bandgap emission is studied by simulating the self-trapping of electron (STE) and holes (STH) in the perfect lattice and trapping of the electron at the bromide vacancy V_{Br} site (Figure 6f). To accurately simulate the electronic structures of the perovskites, the hybrid PBE0 functional[59] has been used by increasing the exact exchange fraction α to 0.29. The use of α=0.29 in combination with a rigid application of SOC provides a band gap of 3.15 eV for BA system, matching the G_0W_0 band gap. SOC is not directly included in PBE0 calculations due to the prohibitive computational cost in supercell calculations. In Table 4 the estimated electronic band gaps at the PBE0-SOC level of theory

for the two systems are reported. As already observed at the PBE-SOC level, the modelled phases show similar band gaps.

In Table 4 the calculated thermodynamic ionization levels (TIL) and predicted PL emissions of trapped electrons and holes in the two phases are reported. Notably, calculated transitions show very similar values in the two perovskites, indicating that they share a comparable defect photo-physics.

Table 4. Estimated electronic band gaps of the $(BA)_4AgBiBr_8$ and $(iBA)_4AgBiBr_8$ perovskites at the PBE0-SOC level (SOC corrections have been rigidly applied to the PBE0 band gap); calculated TIL and PL emissions of self-trapped electron (STE), hole (STH) and trapped electron on V_{Br} defect, at the PBE0 level. All values are in eV.

Compound	**$(BA)_4AgBiBr_8$**		**$(iBA)_4AgBiBr_8$**	
E_g	3.15		3.24	
Defect transition	TIL	PL	TIL	PL
STE (0/-)	3.03	2.03	3.03	2.02
STH (+/0)	0.13	2.59	0.09	2.61
V_{Br} (+/0)	2.27	1.29	2.22	1.25

Self-trapping of the electron, simulated by adding a negative charge in the supercell and relaxing ion positions, leads to the electron localization on one Bi ion and to an elongation of the in-plane Bi-Br bonds from ~2.9 to 3.3 Å (Figure 6f). Electron trapping gives rise to a deep (0/-) thermodynamic transition in the band gap, placed at 3.0 eV above the VB of the perovskites. Radiative decay of the STE with a PL emission at ~2.0 eV is calculated. Simulation of a self-trapped hole (STH) in the pristine system also shows localization of the hole on a single Ag-d orbital hybridized with Br-p orbitals in the cell (Figure 6f). Hole trapping leads to a (+/0) transition placed at 0.1 eV above VB and is accompanied by a slight shortening of the Ag-Br bond distances in the localization site from 2.7 to 2.5 Å. A PL emission from STH is calculated at ~2.6 eV. Electron trapping at the V_{Br}^{+} site leads to a deeper (+/0) transition in the band gap with a predicted PL emission in the low energy range at ~1.2-1.3 eV.

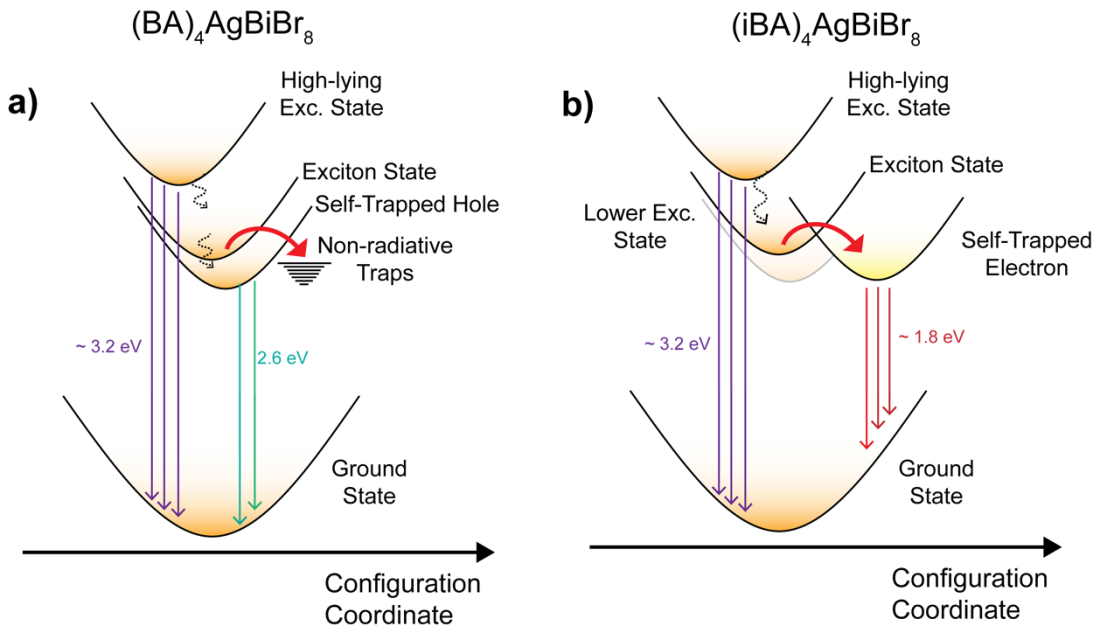

Figure 7. a,b) Schematic representation of the energetic levels in the configuration coordinate picture, summarizing the structure of the excited states for $(BA)_4AgBiBr_8$ and $(iBA)_4AgBiBr_8$, respectively. Colored arrows represent emission signals and dotted lines represent relaxation processes. The parabolas represent the potential energy surfaces of the different states, their position on the x-axis indicates the degree of distortion.

Based on our predictions, the two isomeric perovskites (i.e., iBA and BA-based) show a very similar defect photo-physics and no remarkable differences in PL emissions ascribable to the two isomeric cations can be inferred. By considering the cation-induced distortion and the absorption band splitting also observed in the $(iBA)_4AgBiBr_8$ thin-film absorption, emission peak at ~1.8 eV is safely ascribed to emission from a self-trapped electron states driven by phonon coupling. Namely, as a consequence of the excitation-phonon coupling, excitations are trapped in the lattice distortion that they generate.[60] Similar emissions from self-trapped carriers have been reported for 2D lead halide perovskites and other corrugated metal-halide complexes.[61,62] On the other hand, the emission at 2.6 eV can be assigned to the band-to-band exciton recombination or to STH emission, where only the hole undergoes localization. In Figure 7, we summarize the photophysics of BA and iBA-based model systems, and the assignment discussed above. We expect this picture to provide a guide for future work delving deeper into the photophysics of two-dimensional $(RA)_4AgBiBr_8$ perovskites.

It is worth noting that while ab-initio methods give a unique insight into the photo-physics of these systems, some of our observation differ from predictions. For instance, as already

reported, no STE emission is observed for $(BA)_4AgBiBr_8$. Furthermore, similarly to what observed by Connor et al.,[21] the absorption spectra of thin films do not show strong absorption features at 2.7 eV, which are instead observed for powders. However, we note that extrinsic effects have already demonstrated to be crucial in determining the properties of lower-dimensional lead-halide perovskites.[63] Notably, also the use of corrugated perovskites (obtained via subtle changes in the large cation) has already been proven in white light-emitting 2D lead-based perovskites.[64] While its extent remains an open question, we speculate that morphology could contribute to steering the photophysics of these materials (e.g., by modulating the oscillator strength of some transitions and the carrier-phonon coupling). Such a hypothesis is further confirmed by the significant distribution of WF measured by KPFM on the micro-structured surface of $(iBA)_4AgBiBr_8$. We nevertheless expect that future work will be needed to fully elucidate the impact of morphology on the optical properties of 2D-DHPs.

3. Conclusions

In this work we provide a comprehensive characterization of the structural properties of hydrothermally-synthesized 2D monolayer DHP series, with the general formula $(RA)_4AgBiBr_8$. Here, by using four bulky organic cations (RA) with different alkyl chain length, branching and dipole moments, we finely tuned the inter-layer distances in these silver/bismuth bromide 2D DHP. Interestingly, the nature of the large organic cation also chameleonically determines the thin-film morphologies obtained after a re-crystallization process of the crystalline powders. The resulting different thin-film microstructures span from the case of very flat and homogeneous surfaces, as found for the $(BA)_4AgBiBr_8$ based thin films, to rougher or extremely soft cases (for $(PEA)_4AgBiBr_8$ and $(BA)_4AgBiBr_8$, respectively) up to the formation of complex porous architectures, as found for the $(iBA)_4AgBiBr_8$ thin films. Notably, the simple isomerization to a branched alkyl ammonium cation (i.e. from butylammonium to isobutylammonium) results in an extreme variation of the film morphology. A similar multifaceted nature associated with the mere identity of a small molecular component within a hybrid semiconductor primarily drives structure-property relationships, which here have been characterized mainly in terms of basic optical features. Fine-tuning of structure and morphology of the thin films is proven useful to control the optical properties of 2D DHP. By changing from a linear (BA^+) to a branched (iBA^+) cation, the excitonic recombination is outpaced by a broad and relatively intense STE emission. This interplay between structure, morphology and optical properties provides exciting perspectives not only for delving deeper

into the optical properties of layered metal halide perovskites but also for a material-by-design approach. Our systematic study of large cation effects on structure, morphology, electronic and optical properties lies the foundation for the future development of the 2D DHP material platform. We expect that future effort will be directed in further expanding the nature (i.e., steric hindrance, chemistry, and electronic properties) of large cations, thus following the development of their lead-based counterparts. Although a complete optoelectronic characterization of these materials will require further studies, the map of the excited states in Figure 7 will provide a valuable guide for future investigations.

This work represents a significant step ahead in the field on non-toxic DHP and cast new hopes for the complete substitution of lead in next-generation low-cost optoelectronic devices.

Experimental Section

Materials and methods. All the double perovskite precursors, namely $BiBr_3$(99%), CsBr (99.9%), AgBr (99.5%) were purchased from Alfa Aesar. $BiBr_3$ was stored in a glovebox due to moisture sensitivity and AgBr in dark due to light sensitivity. The crystalline reference 3D double perovskite compound was synthesized through hydrothermal synthesis following a previously reported procedures from some of us.[10] The organic amines were purchased from Sigma Aldrich, as were all solvents. P-XRD analysis was performed at ambient temperature with a PANalytical B.V. X'Pert PRO diffractometer employing CuKα1 radiation. The instrument operated at 40 kV and 40 mA using a 1°divergence slit for the incident beam. SC-XRD was measured at low temperatures (100K) using φ- and ω-scans on a Bruker D8 Venture system equipped with dual IμS microfocus sources, a PHOTON100 detector and an OXFORD CRYOSYSTEMS 700 low-temperature system. Mo-Kα radiation with wavelength 0.71073 Å and a collimating Quazar multilayer mirror were used. Semi-empirical absorption correction from equivalents was applied using SADABS-2016/2[65] and the structures were solved by the dual space algorithm implemented in SHELXT2014/5.[66] Refinement was performed against F^2 on all data by full-matrix least-squares using SHELXL2018/3.[67] All non-hydrogen atoms were refined anisotropically and hydrogen atoms were positioned at geometrically calculated positions and refined using a riding model. The isotropic displacement parameters of all hydrogen atoms were fixed to 1.2x or 1.5x (NH_3 hydrogens) the U_{eq} value of the atoms they are linked to. Disorder was modelled with the help of similarity restraints on bond distances, restraints to a common plane, similarity restraints on anisotropic displacement parameters[68] and advanced rigid bond restraints.[69] Micro-Raman analysis was carried out using a Senterra

Raman microscope equipped with a λ = 532 nm laser. All the measurements were conducted by positioning a small amount of powder on a glass slide, which was placed upon the support inside the instrument. Ethanolic suspensions of the hydrothermally synthesized 2D double perovskites were drop-casted and dried on 200 mesh copper supported lacey carbon grids, and their morphological characteristics were investigated through a FEI Tecnai G2 20 X Twin TEM using 200 kV accelerating voltage (FEI Corporate Headquarters, Hillsboro, OR, USA) followed by the crystal structure analysis of the samples through selected area electron diffraction (SAED). Furthermore, and their chemical composition was assessed by Energy Dispersive X-Ray Spectroscopy (EDS) using a Bruker XFlash 6T-30 detector mounted onto the TEM (Bruker Corporation, Billerica, MA, USA). SEM was performed on a Zeiss Merlin instrument at a working potential of 20 kV. GIXRD was performed in a range of 3° to 70° (0.05° step size, 0.014 °/s scan speed) with a PANalytical B.V. X'Pert Pro diffractometer using Cu Kα1 radiation. The diffraction patterns were measured along the 2θ axis with a grazing incidence of ω = 0.5°. AFM characterization was carried out with a SmartSPM 1000 from AIST-NT in intermittent contact mode using SEIHR probes (NanoWorld). FM-KPFM was measured using a Vacuscope 2000 from AIST-NT at a pressure below 10-6 mbar using OPUS 160AC-GG cold coated silicon probes operated in two-pass mode. The first pass was used to obtain a surface profile while the contact potential difference was obtained following that profile during the second pass by the sideband method using an AC voltage of 2 V at around 1 kHz. Referencing to the known work function of freshly cleaved HOPG ZYA (4.6 eV,[70] MikroMash) was carried out before and after every measurement to avoid the influence of contamination of the probe. UV-vis absorption measurements of thin films were carried out on an Agilent 8453 UV-Vis spectrometer. Diffuse reflectance spectra were acquired on a Cary 5E UV-Vis-NIR spectrometer equipped with a diffuse reflectance accessory. DLS measurements were conducted with a Malvern Zetasizer Nano-ZS device (Malvern, UK) at 20 °C. The DLS system was operated by the Zetasizer software from Malvern Panlytical (Malvern, UK). PL measurements were performed on a HORIBA Jobin Yvon Spex Fluorolog 3 spectrophotometer equipped with a 450 W Xe short-arc lamp, double grated excitation and emission monochromators, and a photomultiplier tube in quartz glass cuvette at 77 K using a special liquid nitrogen-filled Dewar assembly using the FluoroEssence™ software package. Excitation and emission spectra were corrected for the spectral response of the monochromators and the detector using spectral corrections provided by the manufacturer. The dipole moment of isolated RA^+ cations was calculated by DFT using the B3LYP hybrid functional with the basis set 6-31G* following geometry-optimization of the structures.

Hydrothermal synthesis of $(RA)_4AgBiBr_8$ double perovskites. 408 mg of $BiBr_3$ (0.9 mmol) and 170 mg of AgBr (0.9 mmol) were transferred to a two-necked 25 mL round bottom flask. 2.6 mL HBr (49 %) were added with a 5 mL syringe to dissolve inorganic precursors. Last, 3.6 mmol of the primary amine were added with a Labsolute 1000 mL pipet to the stirring mixture, which caused smoke development. The solution was stirred and heated to 100 °C under reflux cooling until all reactants were dissolved. Dissolution occurred between 100 and 120 °C, depending on the amine. While heating, the color of the solution turned from light orange into dark orange. After 30 min, the solutions were cooled down to room temperature. Crystalline materials started to participate as soon as the heating was removed. Products were filtered and washed with diethyl ether several times. Subsequent to washing, the products were dried on filtration paper for a few minutes and then transferred to a weighing boat to continue drying overnight. The drying process proceeded under ambient conditions. Single crystals of $(PEA)_4AgBiBr_8$ were obtained by stratifying diethyl ether on top of a supersaturated solution of the polycrystalline powder in DMF and allowing the two solvents to slowly mix overnight. Crystallographic data for $(PEA)_4AgBiBr_8$ was deposited as CCDC 2031528 at the Cambridge Crystallographic Data Centre.

Preparation of thin-films. Glass and FTO substrates (1.5 x 1.5 cm^2) were cleaned by successive ultrasonication in deionized water, acetone and isopropyl alcohol for 15 minutes each, followed by 15 minutes of UV-Ozone cleaning right before the thin film preparation. The precursor solutions were prepared by dissolving 22 μmol of the respective pre-synthesized 2D double perovskite powder in 90 μL DMF and stirred for 2 hours at room temperature. The thin film casting was conducted in a nitrogen-filled glovebox and was based on the protocol of Connor et al.[21] To prepare the thin films, the substrates were mounted on a spin-coater, evenly covered with 30 μL of precursor solution and spun at 4000 rpm for 40 seconds with an acceleration of 200 rpm/s. After spin-coating, the samples were annealed on a hot plate at 100 °C for 4 minutes.

DFT calculations. The electronic structure of (BA, iBA)$_4AgBiBr_8$ perovskites has been calculated in periodic boundary conditions by using plane waves basis set and pseudopotentials, as implemented in the Quantum Espresso simulation package.[71] The Perdew-Burke-Ernzerhof (PBE) functional[54] and norm-conserving pseudopotentials were used by including spin-orbit coupling (SOC). An energy cutoff on the wavefunctions of 60 Ryd and 4x4x1 k-point grid in the BZ were used. In all cases cell parameters of the phases have been relaxed by using the PBE functional (no SOC included) and including DFTD3 dispersion corrections.[55] By this approach the following equilibrium cell parameters have been obtained:

for BA a=8.19 Å, b=8.05 Å, c=26.78 Å, α=90.0°, β=90.1°, γ=90.0°; for iBA a=8.20 Å, b=8.28 Å, c=25.93 Å, α=90.0°, β=88.9°, γ=90.0°. G_0W_0 and BSE calculations for the BA system have been performed by using the Yambo code[72] on top of PBE-SOC calculations. Due to the prohibitive dimension of the system (460 electrons) a minimal but sufficiently converged computational setup has been adopted (see Table S3 of SI). G_0W_0 calculations have been carried out in the plasmon-pole approximation[73] by using a cutoff of 30 Ry (3 Ry) for the exchange (correlation) part of the self-energy, and by including a total of 2560 bands in the calculation of the dielectric matrix and correlation energy. BSE calculations have been performed on top of QP corrected eigenvalues by using a cutoff of 30 Ry (3 Ry) on the exchange (screening) parts and by including 20 occupied and 20 unoccupied bands. For the screening part the same computational setup employed in G_0W_0 calculations was used. The BSE convergence on the k-point grid has been investigated by performing a BSE scissor operator calculation by enlarging the k-grid up to 6x6x1 (see Figure S23).

Self-trapping and defect calculations have been carried out in the 2x2x1 supercells of BA and iBA by using the CP2K software package.[74] Cell parameters of the supercells have been optimized by using the PBE functional and including DFT-D3 dispersions. Equilibrium structures of self-trapped states and defects have been calculated by fixing cell parameters to the optimized values and relaxing ion positions by using the hybrid PBE0 functional[75] with a fraction of exact exchange α = 0.29, in order to reproduce G_0W_0 band gap of the BA system, and by including van der Waals interactions through the DFT-D3 scheme.[55] Calculations have been carried out with Goedecker-Teter-Hutter pseudopotentials,[76] double-ζ polarized basis sets[77] and a cutoff of 300 Ry for the expansion of the electron density in plane waves. The auxiliary density matrix method with the cFIT auxiliary basis set has been used to accelerate hybrid functional calculations.[78] Thermodynamic ionization levels has been calculated by using the following expression:[79]

$$\varepsilon(q/q') = \frac{E[X^q] - E[X^{q'}]}{q' - q} + \frac{E^q_{corr} - E^{q'}_{corr}}{q' - q} - \varepsilon_{\mathrm{VB}}$$

Where $E[X^q]$ are the energies of self-trapped or defect systems in the different state of charge q, ε_{VB} is the valence band of the pristine system and E^q_{corr} are finite size supercell corrections for charged defects. TILs were corrected by applying Makov-Payne corrections by using the static dielectric tensor of $(BA)_4AgBiBr_8$, i.e. $\varepsilon_{xx}\approx\varepsilon_{yy}=6.8$, $\varepsilon_{zz}=3.6$, estimated by using the approach of Umari et al.[80] PL emission energies have been calculated by simulating vertical

transitions between the excited (trapped) and the ground state of the defects at the excited state equilibrium geometry.

Supporting Information

Optical microscope images of the 2D perovskite crystals, high-wavenumber regions of the Raman spectra, single crystals structure details, thermograms, HR-TEM images and TEM EDX data, thin film XRD patterns, thin films cross-section SEM images, AFM topography images, DLS spectra, calculated dipole moments of the organic cations, diffuse reflectance and PL spectra, further computational details.

Acknowledgements

T.G. thanks the European Commission for financial support with the H2020 FET-PROACTIVE-EIC-07-2020 project LIGHT-CAP (project number 101017821) and the Verband der Chemischen Industrie e.V. for financial support through the "Fonds der Chemischen Industrie". D.S acknowledges financial support by Deutsche Forschungsgemeinschaft (Schl. 340/21-3 and GRK 2204).

References

(1) Green, M. A.; Ho-Baillie, A.; Snaith, H. J. The Emergence of Perovskite Solar Cells. *Nat. Photon.* **2014**, *8*, 506–514. https://doi.org/10.1038/nphoton.2014.134.

(2) Stranks, S. D.; Eperon, G. E.; Grancini, G.; Menelaou, C.; Alcocer, M. J. P.; Leijtens, T.; Herz, L. M.; Petrozza, A.; Snaith, H. J. Electron-Hole Diffusion Lengths Exceeding 1 Micrometer in an Organometal Trihalide Perovskite Absorber. *Science (80-.).* **2013**, *342* (6156), 341 LP – 344. https://doi.org/10.1126/science.1243982.

(3) Wehrenfennig, C.; Eperon, G. E.; Johnston, M. B.; Snaith, H. J.; Herz, L. M. High Charge Carrier Mobilities and Lifetimes in Organolead Trihalide Perovskites. *Adv. Mater.* **2014**, *26*, 1584–1589. https://doi.org/10.1002/adma.201305172.

(4) Green, M.; Dunlop, E.; Hohl-Ebinger, J.; Yoshita, M.; Kopidakis, N.; Hao, X. Solar Cell Efficiency Tables (Version 57). *Prog. Photovoltaics Res. Appl.* **2021**, *29* (1), 3–15. https://doi.org/https://doi.org/10.1002/pip.3371.

(5) Li, J.; Cao, H.-L.; Jiao, W.-B.; Wang, Q.; Wei, M.; Cantone, I.; Lü, J.; Abate, A. Biological Impact of Lead from Halide Perovskites Reveals the Risk of Introducing a Safe Threshold. *Nat. Commun.* **2020**, *11* (1), 310. https://doi.org/10.1038/s41467-019-13910-y.

(6) Zhang, S.; Han, G. Intrinsic and Environmental Stability Issues of Perovskite Photovoltaics.

Prog. Energy **2020**, *2* (2), 22002. https://doi.org/10.1088/2516-1083/ab70d9.

(7) Kim, M.; Alfano, A.; Perotto, G.; Serri, M.; Dengo, N.; Mezzetti, A.; Gross, S.; Prato, M.; Salerno, M.; Rizzo, A.; Sorrentino, R.; Cescon, E.; Meneghesso, G.; Di Fonzo, F.; Petrozza, A.; Gatti, T.; Lamberti, F. Moisture Resistance in Perovskite Solar Cells Attributed to a Water-Splitting Layer. *Commun. Mater.* **2021**, *2* (1), 6. https://doi.org/10.1038/s43246-020-00104-z.

(8) Kangsabanik, J.; Sugathan, V.; Yadav, A.; Yella, A.; Alam, A. Double Perovskites Overtaking the Single Perovskites: A Set of New Solar Harvesting Materials with Much Higher Stability and Efficiency. *Phys. Rev. Mater.* **2018**, *2* (5), 55401. https://doi.org/10.1103/PhysRevMaterials.2.055401.

(9) Jin, Z.; Zhang, Z.; Xiu, J.; Song, H.; Gatti, T.; He, Z. A Critical Review on Bismuth and Antimony Halides Based Perovskites and Derivatives for Photovoltaic Applications: Recent Advances and Challenges. *J. Mater. Chem. A* **2020**, *8*, 16166–16188. https://doi.org/10.1039/D0TA05433J.

(10) Schmitz, F.; Guo, K.; Horn, J.; Sorrentino, R.; Conforto, G.; Lamberti, F.; Brescia, R.; Drago, F.; Prato, M.; He, Z.; Giovanella, U.; Cacialli, F.; Schlettwein, D.; Meggiolaro, D.; Gatti, T. Lanthanide-Induced Photoluminescence in Lead-Free Cs 2 AgBiBr 6 Bulk Perovskite: Insights from Optical and Theoretical Investigations. *J. Phys. Chem. Lett.* **2020**, *11* (20), 8893–8900. https://doi.org/10.1021/acs.jpclett.0c02317.

(11) Fabini, D. H.; Seshadri, R.; Kanatzidis, M. G. The Underappreciated Lone Pair in Halide Perovskites Underpins Their Unusual Properties. *MRS Bull.* **2020**, *45* (6), 467–477. https://doi.org/10.1557/mrs.2020.142.

(12) Righetto, M.; Meggiolaro, D.; Rizzo, A.; Sorrentino, R.; He, Z.; Meneghesso, G.; Sum, T. C.; Gatti, T.; Lamberti, F. Coupling Halide Perovskites with Different Materials: From Doping to Nanocomposites, beyond Photovoltaics. *Prog. Mater. Sci.* **2020**, *110*, 100639. https://doi.org/https://doi.org/10.1016/j.pmatsci.2020.100639.

(13) Zhang, Z.; Liang, Y.; Huang, H.; Liu, X.; Li, Q.; Chen, L.; Xu, D. Stable and Highly Efficient Photocatalysis with Lead-Free Double-Perovskite of Cs2AgBiBr6. *Angew. Chemie Int. Ed.* **2019**, *58* (22), 7263–7267. https://doi.org/https://doi.org/10.1002/anie.201900658.

(14) Liu, G.; Wu, C.; Zhang, Z.; Chen, Z.; Xiao, L.; Qu, B. Ultraviolet-Protective Transparent Photovoltaics Based on Lead-Free Double Perovskites. *Sol. RRL* **2020**, *4* (5), 2000056. https://doi.org/https://doi.org/10.1002/solr.202000056.

(15) Peng, Y.; Huq, T. N.; Mei, J.; Portilla, L.; Jagt, R. A.; Occhipinti, L. G.; MacManus-Driscoll, J. L.; Hoye, R. L. Z.; Pecunia, V. Lead-Free Perovskite-Inspired Absorbers for Indoor

Photovoltaics. *Adv. Energy Mater.* **2021**, *11* (1), 2002761. https://doi.org/https://doi.org/10.1002/aenm.202002761.

(16) Pecunia, V.; Occhipinti, L. G.; Chakraborty, A.; Pan, Y.; Peng, Y. Lead-Free Halide Perovskite Photovoltaics: Challenges, Open Questions, and Opportunities. *APL Mater.* **2020**, *8* (10), 100901. https://doi.org/10.1063/5.0022271.

(17) Pan, W.; Wu, H.; Luo, J.; Deng, Z.; Ge, C.; Chen, C.; Jiang, X.; Yin, W.-J.; Niu, G.; Zhu, L.; Yin, L.; Zhou, Y.; Xie, Q.; Ke, X.; Sui, M.; Tang, J. Cs2AgBiBr6 Single-Crystal X-Ray Detectors with a Low Detection Limit. *Nat. Photonics* **2017**, *11* (11), 726–732. https://doi.org/10.1038/s41566-017-0012-4.

(18) Xing, G.; Wu, B.; Wu, X.; Li, M.; Du, B.; Wei, Q.; Guo, J.; Yeow, E. K. L.; Sum, T. C.; Huang, W. Transcending the Slow Bimolecular Recombination in Lead-Halide Perovskites for Electroluminescence. *Nat. Commun.* **2017**, *8* (1), 14558. https://doi.org/10.1038/ncomms14558.

(19) Giovanni, D.; Ramesh, S.; Righetto, M.; Melvin Lim, J. W.; Zhang, Q.; Wang, Y.; Ye, S.; Xu, Q.; Mathews, N.; Sum, T. C. The Physics of Interlayer Exciton Delocalization in Ruddlesden–Popper Lead Halide Perovskites. *Nano Lett.* **2021**, *21* (1), 405–413. https://doi.org/10.1021/acs.nanolett.0c03800.

(20) Katan, C.; Mercier, N.; Even, J. Quantum and Dielectric Confinement Effects in Lower-Dimensional Hybrid Perovskite Semiconductors. *Chem. Rev.* **2019**, *119* (5), 3140–3192. https://doi.org/10.1021/acs.chemrev.8b00417.

(21) Connor, B. A.; Leppert, L.; Smith, M. D.; Neaton, J. B.; Karunadasa, H. I. Layered Halide Double Perovskites: Dimensional Reduction of Cs2AgBiBr6. *J. Am. Chem. Soc.* **2018**, *140* (15), 5235–5240. https://doi.org/10.1021/jacs.8b01543.

(22) Jana, M. K.; Janke, S. M.; Dirkes, D. J.; Dovletgeldi, S.; Liu, C.; Qin, X.; Gundogdu, K.; You, W.; Blum, V.; Mitzi, D. B. Direct-Bandgap 2D Silver–Bismuth Iodide Double Perovskite: The Structure-Directing Influence of an Oligothiophene Spacer Cation. *J. Am. Chem. Soc.* **2019**, *141* (19), 7955–7964. https://doi.org/10.1021/jacs.9b02909.

(23) Ortiz-Cervantes, C.; Carmona-Monroy, P.; Solis-Ibarra, D. Two-Dimensional Halide Perovskites in Solar Cells: 2D or Not 2D? *ChemSusChem* **2019**, *12* (8), 1560–1575. https://doi.org/10.1002/cssc.201802992.

(24) Yao, Y.; Kou, B.; Peng, Y.; Wu, Z.; Li, L.; Wang, S.; Zhang, X.; Liu, X.; Luo, J. (C3H9NI)4AgBiI8: A Direct-Bandgap Layered Double Perovskite Based on a Short-Chain Spacer Cation for Light Absorption. *Chem. Commun.* **2020**, *56* (21), 3206–3209.

https://doi.org/10.1039/C9CC07796K.

(25) Wang, X.; Li, K.; Xu, H.; Ali, N.; Wang, Y.; Shen, Q.; Wu, H. Synthesis of Large Two-Dimensional Lead-Free Bismuth–Silver Double Perovskite Microplatelets and Their Application for Field-Effect Transistors. *Chem. Commun.* **2020**, *56*, 7917-7920. https://doi.org/10.1039/D0CC01847C.

(26) Martín-García, B.; Spirito, D.; Biffi, G.; Artyukhin, S.; Bonaccorso, F.; Krahne, R. Phase Transitions in Low-Dimensional Layered Double Perovskites: The Role of the Organic Moieties. *J. Phys. Chem. Lett.* **2021**, *12* (1), 280–286. https://doi.org/10.1021/acs.jpclett.0c03275.

(27) Zhang, F.; Lu, H.; Tong, J.; Berry, J. J.; Beard, M. C.; Zhu, K. Advances in Two-Dimensional Organic–Inorganic Hybrid Perovskites. *Energy Environ. Sci.* **2020**, *13* (4), 1154–1186. https://doi.org/10.1039/C9EE03757H.

(28) Khalfin, S.; Bekenstein, Y. Advances in Lead-Free Double Perovskite Nanocrystals, Engineering Band-Gaps and Enhancing Stability through Composition Tunability. *Nanoscale* **2019**, *11* (18), 8665–8679. https://doi.org/10.1039/C9NR01031A.

(29) Cao, D. H.; Stoumpos, C. C.; Farha, O. K.; Hupp, J. T.; Kanatzidis, M. G. 2D Homologous Perovskites as Light-Absorbing Materials for Solar Cell Applications. *J. Am. Chem. Soc.* **2015**, *137* (24), 7843–7850. https://doi.org/10.1021/jacs.5b03796.

(30) Kentsch, R.; Scholz, M.; Horn, J.; Schlettwein, D.; Oum, K.; Lenzer, T. Exciton Dynamics and Electron–Phonon Coupling Affect the Photovoltaic Performance of the Cs2AgBiBr6 Double Perovskite. *J. Phys. Chem. C* **2018**, *122* (45), 25940–25947. https://doi.org/10.1021/acs.jpcc.8b09911.

(31) Li, X.; Fu, Y.; Pedesseau, L.; Guo, P.; Cuthriell, S.; Hadar, I.; Even, J.; Katan, C.; Stoumpos, C. C.; Schaller, R. D.; Harel, E.; Kanatzidis, M. G. Negative Pressure Engineering with Large Cage Cations in 2D Halide Perovskites Causes Lattice Softening. *J. Am. Chem. Soc.* **2020**, *142* (26), 11486–11496. https://doi.org/10.1021/jacs.0c03860.

(32) Yuan, W.; Niu, G.; Xian, Y.; Wu, H.; Wang, H.; Yin, H.; Liu, P.; Li, W.; Fan, J. In Situ Regulating the Order–Disorder Phase Transition in Cs2AgBiBr6 Single Crystal toward the Application in an X-Ray Detector. *Adv. Funct. Mater.* **2019**, *29* (20), 1900234. https://doi.org/https://doi.org/10.1002/adfm.201900234.

(33) Guijarro, A.; Vergés, J. A.; San-Fabián, E.; Chiappe, G.; Louis, E. Herringbone Pattern and CH–π Bonding in the Crystal Architecture of Linear Polycyclic Aromatic Hydrocarbons. *ChemPhysChem* **2016**, *17* (21), 3548–3557.

https://doi.org/https://doi.org/10.1002/cphc.201600586.

(34) Gatti, T.; Brambilla, L.; Tommasini, M.; Villafiorita-Monteleone, F.; Botta, C.; Sarritzu, V.; Mura, A.; Bongiovanni, G.; Zoppo, M. D. Near IR to Red Up-Conversion in Tetracene/Pentacene Host/Guest Cocrystals Enhanced by Energy Transfer from Host to Guest. *J. Phys. Chem. C* **2015**, *119* (31). https://doi.org/10.1021/acs.jpcc.5b01909.

(35) Nicolini, T.; Famulari, A.; Gatti, T.; Martí-Rujas, J.; Villafiorita-Monteleone, F.; Canesi, E. V.; Meinardi, F.; Botta, C.; Parisini, E.; Meille, S. V.; Bertarelli, C. Structure-Photoluminescence Correlation for Two Crystalline Polymorphs of a Thiophene-Phenylene Co-Oligomer with Bulky Terminal Substituents. *J. Phys. Chem. Lett.* **2014**, *5* (13). https://doi.org/10.1021/jz500925r.

(36) Liu, Y.; Siron, M.; Lu, D.; Yang, J.; dos Reis, R.; Cui, F.; Gao, M.; Lai, M.; Lin, J.; Kong, Q.; Lei, T.; Kang, J.; Jin, J.; Ciston, J.; Yang, P. Self-Assembly of Two-Dimensional Perovskite Nanosheet Building Blocks into Ordered Ruddlesden–Popper Perovskite Phase. *J. Am. Chem. Soc.* **2019**, *141* (33), 13028–13032. https://doi.org/10.1021/jacs.9b06889.

(37) Xu, Y.; Wang, M.; Lei, Y.; Ci, Z.; Jin, Z. Crystallization Kinetics in 2D Perovskite Solar Cells. *Adv. Energy Mater.* **2020**, *10* (43), 2002558. https://doi.org/https://doi.org/10.1002/aenm.202002558.

(38) Quintero-Bermudez, R.; Gold-Parker, A.; Proppe, A. H.; Munir, R.; Yang, Z.; Kelley, S. O.; Amassian, A.; Toney, M. F.; Sargent, E. H. Compositional and Orientational Control in Metal Halide Perovskites of Reduced Dimensionality. *Nat. Mater.* **2018**, *17* (10), 900–907. https://doi.org/10.1038/s41563-018-0154-x.

(39) Zuo, C.; Scully, A. D.; Tan, W. L.; Zheng, F.; Ghiggino, K. P.; Vak, D.; Weerasinghe, H.; McNeill, C. R.; Angmo, D.; Chesman, A. S. R.; Gao, M. Crystallisation Control of Drop-Cast Quasi-2D/3D Perovskite Layers for Efficient Solar Cells. *Commun. Mater.* **2020**, *1* (1), 33. https://doi.org/10.1038/s43246-020-0036-z.

(40) Wang, J.; Luo, S.; Lin, Y.; Chen, Y.; Deng, Y.; Li, Z.; Meng, K.; Chen, G.; Huang, T.; Xiao, S.; Huang, H.; Zhou, C.; Ding, L.; He, J.; Huang, J.; Yuan, Y. Templated Growth of Oriented Layered Hybrid Perovskites on 3D-like Perovskites. *Nat. Commun.* **2020**, *11* (1), 582. https://doi.org/10.1038/s41467-019-13856-1.

(41) Pratap, S.; Schlipf, J.; Bießmann, L.; Müller-Buschbaum, P. Hierarchical Structures from Nanocrystalline Colloidal Precursors within Hybrid Perovskite Thin Films: Implications for Photovoltaics. *ACS Appl. Nano Mater.* **2020**, *3* (12), 11701–11708. https://doi.org/10.1021/acsanm.0c03000.

(42) Yang, J.; Xiong, S.; Song, J.; Wu, H.; Zeng, Y.; Lu, L.; Shen, K.; Hao, T.; Ma, Z.; Liu, F.; Duan, C.; Fahlman, M.; Bao, Q. Energetics and Energy Loss in 2D Ruddlesden–Popper Perovskite Solar Cells. *Adv. Energy Mater.* **2020**, *10* (23), 2000687. https://doi.org/https://doi.org/10.1002/aenm.202000687.

(43) Meggiolaro, D.; Mosconi, E.; Proppe, A. H.; Quintero-Bermudez, R.; Kelley, S. O.; Sargent, E. H.; De Angelis, F. Energy Level Tuning at the MAPbI3 Perovskite/Contact Interface Using Chemical Treatment. *ACS Energy Lett.* **2019**, *4* (9), 2181–2184. https://doi.org/10.1021/acsenergylett.9b01584.

(44) Bekenstein, Y.; Dahl, J. C.; Huang, J.; Osowiecki, W. T.; Swabeck, J. K.; Chan, E. M.; Yang, P.; Alivisatos, A. P. The Making and Breaking of Lead-Free Double Perovskite Nanocrystals of Cesium Silver–Bismuth Halide Compositions. *Nano Lett.* **2018**, *18* (6), 3502–3508. https://doi.org/10.1021/acs.nanolett.8b00560.

(45) Schmitz, A.; Schaberg, L. L.; Sirotinskaya, S.; Pantaler, M.; Lupascu, D. C.; Benson, N.; Bacher, G. Fine Structure of the Optical Absorption Resonance in Cs2AgBiBr6 Double Perovskite Thin Films. *ACS Energy Lett.* **2020**, *5* (2), 559–565. https://doi.org/10.1021/acsenergylett.9b02781.

(46) Palummo, M.; Berrios, E.; Varsano, D.; Giorgi, G. Optical Properties of Lead-Free Double Perovskites by Ab Initio Excited-State Methods. *ACS Energy Lett.* **2020**, *5* (2), 457–463. https://doi.org/10.1021/acsenergylett.9b02593.

(47) Zelewski, S. J.; Urban, J. M.; Surrente, A.; Maude, D. K.; Kuc, A.; Schade, L.; Johnson, R. D.; Dollmann, M.; Nayak, P. K.; Snaith, H. J.; Radaelli, P.; Kudrawiec, R.; Nicholas, R. J.; Plochocka, P.; Baranowski, M. Revealing the Nature of Photoluminescence Emission in the Metal-Halide Double Perovskite Cs2AgBiBr6. *J. Mater. Chem. C* **2019**, *7* (27), 8350–8356. https://doi.org/10.1039/C9TC02402F.

(48) Schade, L.; Wright, A. D.; Johnson, R. D.; Dollmann, M.; Wenger, B.; Nayak, P. K.; Prabhakaran, D.; Herz, L. M.; Nicholas, R.; Snaith, H. J.; Radaelli, P. G. Structural and Optical Properties of Cs2AgBiBr6 Double Perovskite. *ACS Energy Lett.* **2019**, *4* (1), 299–305. https://doi.org/10.1021/acsenergylett.8b02090.

(49) Righetto, M.; Lim, S. S.; Giovanni, D.; Lim, J. W. M.; Zhang, Q.; Ramesh, S.; Tay, Y. K. E.; Sum, T. C. Hot Carriers Perspective on the Nature of Traps in Perovskites. *Nat. Commun.* **2020**, *11* (1), 2712. https://doi.org/10.1038/s41467-020-16463-7.

(50) Righetto, M.; Privitera, A.; Fortunati, I.; Mosconi, D.; Zerbetto, M.; Curri, M. L.; Corricelli, M.; Moretto, A.; Agnoli, S.; Franco, L.; Bozio, R.; Ferrante, C. Spectroscopic Insights into

Carbon Dot Systems. *J. Phys. Chem. Lett.* **2017**, *8* (10), 2236–2242. https://doi.org/10.1021/acs.jpclett.7b00794.

(51) Righetto, M.; Minotto, A.; Bozio, R. Bridging Energetics and Dynamics of Exciton Trapping in Core–Shell Quantum Dots. *J. Phys. Chem. C* **2017**, *121* (1), 896–902. https://doi.org/10.1021/acs.jpcc.6b10146.

(52) Kasha, M. Characterization of Electronic Transitions in Complex Molecules. *Discuss. Faraday Soc.* **1950**, *9* (0), 14–19. https://doi.org/10.1039/DF9500900014.

(53) Li, B.; Brosseau, P. J.; Strandell, D. P.; Mack, T. G.; Kambhampati, P. Photophysical Action Spectra of Emission from Semiconductor Nanocrystals Reveal Violations to the Vavilov Rule Behavior from Hot Carrier Effects. *J. Phys. Chem. C* **2019**, *123* (8), 5092–5098. https://doi.org/10.1021/acs.jpcc.8b11218.

(54) Perdew, J. P.; Burke, K.; Ernzerhof, M. Generalized Gradient Approximation Made Simple. *Phys. Rev. Lett.* **1996**, *77*, 3865–3868. https://doi.org/10.1103/PhysRevLett.77.3865.

(55) Grimme, S.; Antony, J.; Ehrlich, S.; Krieg, H. A Consistent and Accurate Ab Initio Parametrization of Density Functional Dispersion Correction (DFT-D) for the 94 Elements H-Pu. *J. Chem. Phys.* **2010**, *132* (15), 154104. https://doi.org/10.1063/1.3382344.

(56) Hybertsen, M. S.; Louie, S. G. Electron Correlation in Semiconductors and Insulators: Band Gaps and Quasiparticle Energies. *Phys. Rev. B* **1986**, *34* (8), 5390–5413. https://doi.org/10.1103/PhysRevB.34.5390.

(57) Onida, G.; Reining, L.; Rubio, A. Electronic Excitations: Density-Functional versus Many-Body Green's-Function Approaches. *Rev. Mod. Phys.* **2002**, *74* (2), 601–659. https://doi.org/10.1103/RevModPhys.74.601.

(58) Righetto, M.; Giovanni, D.; Lim, S. S.; Sum, T. C. The Photophysics of Ruddlesden-Popper Perovskites: A Tale of Energy, Charges, and Spins. *Appl. Phys. Rev.* **2021**, *8* (1), 11318. https://doi.org/10.1063/5.0031821.

(59) Perdew, J. P.; Ernzerhof, M.; Burke, K. Rationale for Mixing Exact Exchange with Density Functional Approximations. *J. Chem. Phys.* **1996**, *105*, 9982–9985. https://doi.org/doi:http://dx.doi.org/10.1063/1.472933.

(60) Li, S.; Luo, J.; Liu, J.; Tang, J. Self-Trapped Excitons in All-Inorganic Halide Perovskites: Fundamentals, Status, and Potential Applications. *J. Phys. Chem. Lett.* **2019**, *10* (8), 1999–2007. https://doi.org/10.1021/acs.jpclett.8b03604.

(61) Smith, M. D.; Karunadasa, H. I. White-Light Emission from Layered Halide Perovskites. *Acc.*

Chem. Res. **2018**, *51* (3), 619–627. https://doi.org/10.1021/acs.accounts.7b00433.

(62) Febriansyah, B.; Neo, C. S. D.; Giovanni, D.; Srivastava, S.; Lekina, Y.; Koh, T. M.; Li, Y.; Shen, Z. X.; Asta, M.; Sum, T. C.; Mathews, N.; England, J. Targeted Synthesis of Trimeric Organic–Bromoplumbate Hybrids That Display Intrinsic, Highly Stokes-Shifted, Broadband Emission. *Chem. Mater.* **2020**, *32* (11), 4431–4441. https://doi.org/10.1021/acs.chemmater.9b03925.

(63) Kahmann, S.; Tekelenburg, E. K.; Duim, H.; Kamminga, M. E.; Loi, M. A. Extrinsic Nature of the Broad Photoluminescence in Lead Iodide-Based Ruddlesden–Popper Perovskites. *Nat. Commun.* **2020**, *11* (1), 2344. https://doi.org/10.1038/s41467-020-15970-x.

(64) Febriansyah, B.; Giovanni, D.; Ramesh, S.; Koh, T. M.; Li, Y.; Sum, T. C.; Mathews, N.; England, J. Inducing Formation of a Corrugated, White-Light Emitting 2D Lead-Bromide Perovskite via Subtle Changes in Templating Cation. *J. Mater. Chem. C* **2020**, *8* (3), 889–893. https://doi.org/10.1039/C9TC05357C.

(65) Krause, L.; Herbst-Irmer, R.; Sheldrick, G. M.; Stalke, D. Comparison of Silver and Molybdenum Microfocus X-Ray Sources for Single-Crystal Structure Determination. *J. Appl. Crystallogr.* **2015**, *48* (1), 3–10. https://doi.org/10.1107/S1600576714022985.

(66) Sheldrick, G. M. {\it SHELXT} {--} Integrated Space-Group and Crystal-Structure Determination. *Acta Crystallogr. Sect. A* **2015**, *71* (1), 3–8. https://doi.org/10.1107/S2053273314026370.

(67) Sheldrick, G. M. Crystal Structure Refinement with {\it SHELXL}. *Acta Crystallogr. Sect. C* **2015**, *71* (1), 3–8. https://doi.org/10.1107/S2053229614024218.

(68) Müller, P. Practical Suggestions for Better Crystal Structures. *Crystallogr. Rev.* **2009**, *15* (1), 57–83. https://doi.org/10.1080/08893110802547240.

(69) Thorn, A.; Dittrich, B.; Sheldrick, G. M. Enhanced Rigid-Bond Restraints. *Acta Crystallogr. Sect. A* **2012**, *68* (4), 448–451. https://doi.org/10.1107/S0108767312014535.

(70) Fernández Garrillo, P. A.; Grévin, B.; Chevalier, N.; Borowik, Ł. Calibrated Work Function Mapping by Kelvin Probe Force Microscopy. *Rev. Sci. Instrum.* **2018**, *89* (4), 43702. https://doi.org/10.1063/1.5007619.

(71) Giannozzi, P.; Baroni, S.; Bonini, N.; Calandra, M.; Car, R.; Cavazzoni, C.; Ceresoli, D.; Chiarotti, G. L.; Cococcioni, M.; Dabo, I.; Dal Corso, A.; de Gironcoli, S.; Fabris, S.; Fratesi, G.; Gebauer, R.; Gerstmann, U.; Gougoussis, C.; Kokalj, A.; Lazzeri, M.; Martin-Samos, L.; Marzari, N.; Mauri, F.; Mazzarello, R.; Paolini, S.; Pasquarello, A.; Paulatto, L.; Sbraccia, C.;

Scandolo, S.; Sclauzero, G.; Seitsonen, A. P.; Smogunov, A.; Umari, P.; Wentzcovitch, R. M. QUANTUM ESPRESSO: A Modular and Open-Source Software Project for Quantum Simulations of Materials. *J. Phys. Condens. Matter* **2009**, *21* (39), 395502. https://doi.org/10.1088/0953-8984/21/39/395502.

(72) Marini, A.; Hogan, C.; Grüning, M.; Varsano, D. Yambo: An Ab Initio Tool for Excited State Calculations. *Comput. Phys. Commun.* **2009**, *180* (8), 1392–1403. https://doi.org/https://doi.org/10.1016/j.cpc.2009.02.003.

(73) Godby, R. W.; Needs, R. J. Metal-Insulator Transition in Kohn-Sham Theory and Quasiparticle Theory. *Phys. Rev. Lett.* **1989**, *62* (10), 1169–1172. https://doi.org/10.1103/PhysRevLett.62.1169.

(74) VandeVondele, J.; Krack, M.; Mohamed, F.; Parrinello, M.; Chassaing, T.; Hutter, J. Quickstep: Fast and Accurate Density Functional Calculations Using a Mixed Gaussian and Plane Waves Approach. *Comput. Phys. Commun.* **2005**, *167* (2), 103–128. https://doi.org/https://doi.org/10.1016/j.cpc.2004.12.014.

(75) Adamo, C.; Barone, V. Toward Reliable Density Functional Methods without Adjustable Parameters: The PBE0 Model. *J. Chem. Phys.* **1999**, *110* (13), 6158–6170. https://doi.org/10.1063/1.478522.

(76) Goedecker, S.; Teter, M.; Hutter, J. Separable Dual-Space Gaussian Pseudopotentials. *Phys. Rev. B* **1996**, *54* (3), 1703–1710. https://doi.org/10.1103/PhysRevB.54.1703.

(77) VandeVondele, J.; Hutter, J. Gaussian Basis Sets for Accurate Calculations on Molecular Systems in Gas and Condensed Phases. *J. Chem. Phys.* **2007**, *127* (11), 114105. https://doi.org/10.1063/1.2770708.

(78) Guidon, M.; Hutter, J.; VandeVondele, J. Auxiliary Density Matrix Methods for Hartree−Fock Exchange Calculations. *J. Chem. Theory Comput.* **2010**, *6* (8), 2348–2364. https://doi.org/10.1021/ct1002225.

(79) Van de Walle, C. G.; Neugebauer, J. First-Principles Calculations for Defects and Impurities: Applications to III-Nitrides. *J. Appl. Phys.* **2004**, *95*, 3851–3879. https://doi.org/doi:http://dx.doi.org/10.1063/1.1682673.

(80) Umari, P.; Pasquarello, A. Ab Initio Molecular Dynamics in a Finite Homogeneous Electric Field. *Phys. Rev. Lett.* **2002**, *89* (15), 157602. https://doi.org/10.1103/PhysRevLett.89.157602.

TOC Graphic

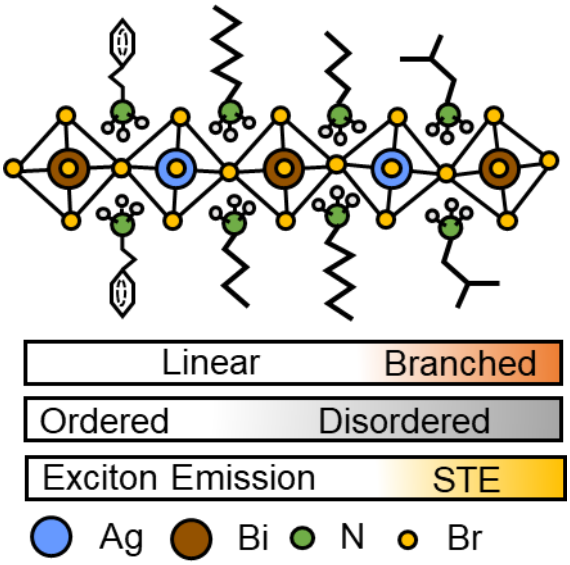
Linear
Branched
Ordered
Disordered
Exciton Emission
STE
Ag
Bi
N
Br